



Oxidation kinetics of overstoichiometric TiB₂ thin films grown by DC magnetron sputtering

Samira Dorri^a, Justinas Palisaitis^a, Grzegorz Greczynski^a, Ivan Petrov^{a,b,c}, Jens Birch^a, Lars Hultman^a, Babak Bakht^{a,*}

^a Thin Film Physics Division, Department of Physics (IFM), Linköping University, Linköping SE-58183, Sweden

^b Materials Research Laboratory and Department of Materials Science, University of Illinois at Urbana-Champaign, Illinois 61801, USA

^c Department of Materials Science and Engineering, National Taiwan University of Science and Technology, Taipei 10607, Taiwan

ARTICLE INFO

Keywords:

Sputtering
Thin films
Titanium diboride (TiB₂)
Microstructure
Oxidation

ABSTRACT

We systematically study the oxidation properties of sputter-deposited TiB_{2.5} coatings up to 700 °C. Oxide-scale thickness d_{ox} increases linearly with time t_a for 300, 400, 500, and 700 °C, while an oxidation-protective behavior occurs with $d_{ox} = 250 \cdot t_a^{0.2}$ at 600 °C. Oxide-layer's structure changes from amorphous to rutile/anatase-TiO₂ at temperatures ≥ 500 °C. Abnormally low oxidation rate at 600 °C is attributed to a highly dense columnar TiO₂-sublayer growing near oxide/film interface with a top-amorphous thin layer, suppressing oxygen diffusion. A model is proposed to explain the oxide-scale evolution at 600 °C. Decreasing heating rate to 1.0 °C/min plays a noticeable role in the TiB_{2.5} oxidation.

1. Introduction

Materials containing boron are subject of growing interest in a broad range of applications. Boron barely follows the octet rule and places six electrons into its valence shell. This peculiarity has a considerable effect on its chemistry and provides a high tendency to form covalent bonding [1,2]. A particular class of boron-containing materials are transition metal diborides (TMB₂) that typically crystallize in a hexagonal AlB_2 -type structure (P6/mmm, SG-191), in which the B atoms form sheets between the hexagonal-close-packed TM layers [2–4]. TMB₂ exhibit a unique combination of properties such as high melting points, excellent hardness, good corrosion and wear resistance, relatively low electrical resistivity, and high thermal and chemical stability [2,5]. These properties, which mostly originate from the dual ceramic/metallic chemical-bonding nature of TMB₂ – strong covalent bonding between TM and B atoms and within the B sheets as well as metallic bonding within TM layers [6,7], make them promising candidates for many strategic applications, especially in extreme thermal and chemical environments, such as rockets [8,9], advanced nuclear fission reactors [5,10], hypersonic aerospace vehicles [9,11], optoelectronic and micro-electronic components [12–14], armor applications, and protective coatings [15–19].

The ever-increasing demand for enhanced coating properties

motivates the search for advanced materials with distinctive functionalities. In this context, TMB₂ thin films grown by magnetron sputtering have recently received increasing attention as the future class of refractory, hard ceramic protective coatings. However, compared to nitrides that have many industrial applications [20–23], the use of the sputter-deposited TM diboride thin films is limited due mainly to their high brittleness [17] and poor oxidation resistance [16]. The TMB₂ coatings are inherently hard, with nanoindentation hardness values ranging from 30 to 50 GPa [19,24–26], but this alone is not sufficient to prevent failure in applications involving high stresses since hardness is usually accompanied by brittleness [27]. To avoid brittle cracking, the TMB₂ thin films need to have both high hardness and ductility, referred to as toughness [28], which can be enhanced by alloying. For example, hard Zr-Cr-B alloy films grown by hybrid high-power impulse and DC magnetron co-sputtering (Cr-HiPIMS/ZrB₂-DCMS) showed higher toughness and consequently better tribological properties compared to ZrB₂ thin films grown by DCMS [29,30]. Zr-Ta-B alloys, with a self-organized columnar core/shell nanostructure [31], exhibited a simultaneous increase in both nanoindentation hardness (from 35 to 42 GPa) and toughness (4.0–5.2 MPa \sqrt{m}) [17] as well as high thermal and mechanical stabilities [19].

In addition, the applications of sputter-deposited TMB₂ coatings are restricted due to their poor oxidation resistance, which is a critical

* Corresponding author.

E-mail address: babak.bakht@liu.se (B. Bakht).

<https://doi.org/10.1016/j.corsci.2022.110493>

Received 6 April 2022; Received in revised form 11 July 2022; Accepted 13 July 2022

Available online 19 July 2022

0010-938X/© 2022 The Author(s). Published by Elsevier Ltd. This is an open access article under the CC BY license (<http://creativecommons.org/licenses/by/4.0/>).

property for many aggressive environments [11]. In general, oxidation products formed on bulk TMb_2 , mostly synthesized by powder metallurgy processes [11,32], at temperatures $T_a \leq 1000^\circ\text{C}$ typically consist of a porous, crystalline TiO_2 (s) phase filled with a glassy, amorphous B_2O_3 (l) [33]. In this temperature range, the B_2O_3 (l) phase has a high wettability [34,35] and forms a continuous B_2O_3 (l) layer on the surface of the oxide scales [36,37] that acts as a barrier for oxygen diffusion and determines the oxidation-rate limit [38]. However, the oxidation properties change at higher temperatures ($T_a \geq 1000^\circ\text{C}$); the B_2O_3 (l) phase rapidly evaporates that results in the formation of a porous TiO_2 (s) skeleton [33,39]. The oxidation kinetics in this temperature regime are controlled by the oxygen transfer rate through the porous oxide scale [40]. The high-temperature oxidation properties of bulk TMb_2 have been widely studied, and it is demonstrated that their oxidation resistance can be significantly increased by adding secondary phases [41]. For example, ZrB_2 containing $\sim 20\%$ SiC showed much higher oxidation resistance than ZrB_2 up to 1600°C [41,42].

We recently showed that the problems with poor oxidation resistance of TM-based diborides (TMb_x) are even worse for the sputter-deposited overstoichiometric (B/TM ratios $x > 2$) diboride thin films. The B_2O_3 (l) phase did not form even at low temperatures, and the oxide scales were mainly composed of the porous TiO_2 (s) phase, which caused a poor oxidation resistance at 700°C [16]. We also showed that the oxidation rate of sputter-deposited TiB_2 can be changed by the B concentration. For instance, the low-temperature oxidation rate of overstoichiometric $\text{TiB}_{2.20}$ and $\text{TiB}_{2.70}$ thin films was considerably higher than that of understoichiometric $\text{TiB}_{1.43}$ [43]. The oxidation resistance was enhanced by alloying with Al, which resulted in the formation of a protective Al-containing oxide scale on the surface of Ti-Al-B alloy films that significantly decreased the oxygen diffusion rate [16,44,45]. Glechner et al. [46] studied the influence of adding Si on the oxidation resistance of different sputter-deposited diboride thin films (TM = Ti, Cr, Hf, Ta, and W). All TM-Si-B alloy coatings showed lower oxidation rates compared to reference monolithic TMb_x thin films. The Hf- and Cr-based alloys had drastically retarded oxidation kinetics than other alloy films due to the formation of an amorphous Si-rich oxide scale.

Although much work has been done on characterizing the microstructure of the sputter-deposited TMb_2 thin films and enhancing their mechanical properties [47–50], little is known about their oxidation mechanisms. Here, we systematically study the oxidation properties and kinetics of $\text{TiB}_{2.5}$ thin films, as TiB_x is the most investigated sputter-deposited diboride coating system, up to $T_a = 700^\circ\text{C}$ with air-annealing times t_a ranging from 1 to 120 h. The films reveal unexpected oxidation rates at $T_a = 500$ and 600°C . $\text{TiB}_{2.5}$ undergo rapid oxidation at $T_a = 500^\circ\text{C}$, while their oxidation rate is abnormally low at $T_a = 600^\circ\text{C}$. We also found that decreasing the heating rate (β) from $10.0^\circ\text{C}/\text{min}$ to $1.0^\circ\text{C}/\text{min}$ plays a significant role in the diboride coating oxidation.

2. Material and methods

The thin films are grown in a CC800/9 CemeCon AG sputtering system equipped with a TiB_2 target ($8.8 \times 50 \text{ cm}^2$). Si(001) substrates are cleaned in acetone and isopropyl alcohol. Then, the substrates are mounted in the deposition chamber facing the TiB_2 target. The distance between target and substrate is 20 cm. The base pressure in the chamber is 3.0×10^{-6} Torr (0.4×10^{-3} Pa), while the deposition pressure during deposition is 3.0 mTorr (0.4 Pa). The TiB_x thin films are grown by DCMS with a TiB_2 -target power of 4000 W, at a substrate temperature of $\sim 500^\circ\text{C}$, and a negative DC substrate potential of 100 V.

A Zeiss LEO 1550 scanning electron microscope (SEM) is employed for examining the surface and fracture cross sections of as-deposited thin films. The cross-sectional and plan-view transmission electron microscopy (TEM) of as-deposited and air-annealed layers are carried out in a FEI Titan³ 60–300 electron microscope. The scanning TEM high-angle-annular-dark-field (STEM-HAADF) mode is used to obtain Z-contrast

images. Electron energy-loss spectroscopy (EELS) elemental maps are also acquired using a GIF Quantum ERS spectrometer in the FEI microscope. TEM specimens are prepared by focused ion beam (FIB) in a Carl Zeiss Cross-Beam 1540 EsB system [51].

The crystal structure and orientation of as-deposited and air-annealed thin films are obtained from X-ray diffraction (XRD) θ -2 θ scans carried out in a Philips X'Pert X-ray diffractometer (using a $\text{Cu K}\alpha$ source with $\lambda = 0.15406 \text{ nm}$). In addition, the substrate radius of curvature (R_s), required for measuring the residual stress of as-deposited TiB_x based on Stoney equation [52,53], is determined from a rocking-curve measurement using a PANalytical Empyrean high-resolution X-ray diffractometer operated at 45 kV and 40 mA.

The chemical compositions and depth profiles of as-deposited and air-annealed TiB_x thin films are determined by time-of-flight elastic recoil detection analysis (ToF-ERDA) in a tandem accelerator with a 36 MeV $^{127}\text{I}^{8+}$ probe beam. More details about the measurements and analyses are given in reference [54]. The chemistry of oxide scales is analyzed using X-ray photoelectron spectroscopy (XPS) in a Kratos Axis Ultra DLD instrument employing monochromatic Al $\text{K}\alpha$ radiation with $h\nu = 1486.6 \text{ eV}$. XPS depth profiles are acquired by sputter-etching with 0.5-keV Ar^+ ions. The ISO-certified procedure is followed to calibrate binding energy scales [55]. As a charge reference, the Fermi edge recorded from sputter-etched $\text{TiB}_{2.5}$ films is used in order to avoid uncertainties associated with employing the C 1 s peak from adventitious carbon [56]. Spectra from oxide layers, in which the Fermi edge is absent, are aligned against the common spectral features that appear in Ti 2p spectra from the oxide/film transition layer. The XPS depth scales are converted from time to distance employing the sputter-etching rate of as-deposited TiB_x and the average film thickness, which is measured by SEM. The nanoindentation analysis of the as-deposited TiB_x thin film is carried out in an Ultra-Micro Indentation System with a sharp Berkovich diamond tip. For determining the hardness of the layer, the load is increased in a range of 5–30 mN with 0.5 mN increments. The obtained values are analyzed according to the Oliver and Pharr method [57].

Isothermal air-annealing experiments are carried out at temperatures $T_a = 300, 400, 500, 600$, and 700°C in a laboratory atmosphere with $\sim 40\%$ humidity. The TiB_x samples grown on Si(001) substrates are air-annealed in a GSL-1100 \times -S furnace from MTI Corporation with a constant heating rate (β) of $10.0^\circ\text{C}/\text{min}$, held at T_a for times t_a up to 120 h, and finally cooled down to room temperature with $\beta = 10.0^\circ\text{C}/\text{min}$. In a few experiments, the samples are air-annealed with $\beta = 5.0$ and $1.0^\circ\text{C}/\text{min}$ to examine the influence of thermal history (heating-up duration from room temperature to T_a) on the morphology and thickness of oxide scales. A separate as-deposited sample is used for each experiment. SEM is used to examine the surface and cross-sectional morphologies of air-annealed samples. The thicknesses of oxide scales formed after air-annealing are also determined using SEM. The oxide growth kinetics of the TiB_x thin films are further studied in the same laboratory atmosphere using a combination of thermogravimetric (TG) and differential scanning calorimetry (DSC) analyses in a STA 449F3 Thermal Analysis System (NETZSCH Co., Germany). Two types of powders are used; TiB_x powders extracted from the TiB_x thin films and TiB_2 powders with the particle size $< 10 \mu\text{m}$ (CAS: 12045–63–5, provided by SIGMA-ALDRICH Germany) as the reference stoichiometric sample. For these measurements, the TiB_x thin films are grown on Fe-foils with the same deposition parameters as the layers on the Si(001) substrates and then detached from the Fe-foils through a substrate-etching process in a hydrochloride acid. The remaining material is filtered, cleaned in de-ionized water, air-dried, and grounded to fine TiB_x powders. Prior to each measurement, the powders are loaded in an alumina crucible and isothermally dried at 150°C in a pure Ar atmosphere for 1 h in the DSC furnace. The dynamic air-annealing measurements are carried out with different heating rates β varying from 1.0° to $40.0^\circ\text{C}/\text{min}$. In addition, the dynamic experiments under the same measurement conditions as the TiB_x powders, but with empty crucibles, are carried out to achieve appropriate baseline corrections.

The isothermal air-annealing measurements are performed with $\beta = 10.0$ °C/min in a pure Ar atmosphere to reach the desired T_a . Then, the powders are isothermally air-annealed for $t_a = 12$ h and eventually cooled down to room temperature.

3. Results

3.1. Composition and microstructure of as-deposited TiB_x

According to ToF-ERDA, the as-deposited TiB_x thin film, with a thickness of 4000 ± 80 nm, contains 70.3 ± 1.2 at% B and 28.2 ± 0.6 at% Ti, representing an overstoichiometric layer with the B/Ti ratio x of ~ 2.5 . The concentrations of C, N, O, and Ar in $TiB_{2.5}$ are 0.3 ± 0.1 at%, 0.5 ± 0.1 at%, 0.4 ± 0.1 at%, and 0.4 ± 0.1 at%, respectively. The cross-sectional and plan-view SEM and bright-field TEM images of as-deposited $TiB_{2.5}$ are shown in Fig. 1. The cross-sectional SEM (XSEM) image, Fig. 1(a), shows that the $TiB_{2.5}$ thin film has a dense, columnar microstructure with columns extending through the layer, and the plan-view SEM image in Fig. 1(b) indicates that the film has a featureless, smooth surface. Both cross-sectional and plan-view TEM micrographs in Fig. 1(c) and 1(d) reveal that the as-deposited film consists of dense columns with no discernable porosity and open boundaries. The layer exhibits a competitive growth in which fine columns are formed near the substrate (up to a thickness of 500 ± 16 nm), while at thicknesses $> 500 \pm 16$ nm, indicated by a horizontal dashed line in Fig. 1(c), fewer columns grow and become wider. At this growth stage, the column width does not change significantly, and the columns extend along the growth direction. Cross-sectional selected-area electron diffraction (SAED) patterns obtained from areas close to the substrate and the film's surface, insets in Fig. 1(c), are composed of strong (001) and (002)

diffraction components. The diffraction components close to the substrate have arc shapes, while those near the film's surface appear like spots indicating more pronounced (001) fiber texture as the film thickness increases.

Fig. 2 comprises the plan-view HAADF-STEM micrograph with corresponding EELS elemental maps of the as-deposited $TiB_{2.5}$ thin film acquired from an area close to the film's surface. The plan-view HAADF-STEM micrograph in Fig. 2(a) shows that the film consists of nanocolumns with a column width of 8.5 ± 2 nm. There is a contrast difference between columns and column boundaries; the columns appear bright, while the column boundaries are dark. These dark regions can correspond to low-Z rich areas [58]. The Ti-L_{2,3} EELS map in Fig. 2(b) reveals that the dark column boundaries are Ti-deficient, while the B-K EELS map confirms that the column boundaries are B-rich compared to the columns. This columnar nanostructure with B-rich column boundaries is typical for sputter-deposited overstoichiometric diborides [17, 25, 48].

The in-plane residual stress σ_f of as-deposited $TiB_{2.5}$ is determined based on the modified Stoney equation [52,53];

$$\sigma_f = (M_s h_s^2) / (6 R_s h_f), \quad (1)$$

where σ_f is the average biaxial stress; h_f and h_s are film and substrate thicknesses, respectively; R_s is the substrate radius of curvature; and M_s is the substrate biaxial modulus, which is 30.05 GPa for Si. The σ_f value is corrected for thermal stresses σ_{th} due to cooling the samples from deposition temperature to room temperature, $\Delta T = 475$ K, using the equation [59]:

$$\sigma_{th} = [E(\alpha_f - \alpha_s)\Delta T] / (1 - \nu), \quad (2)$$

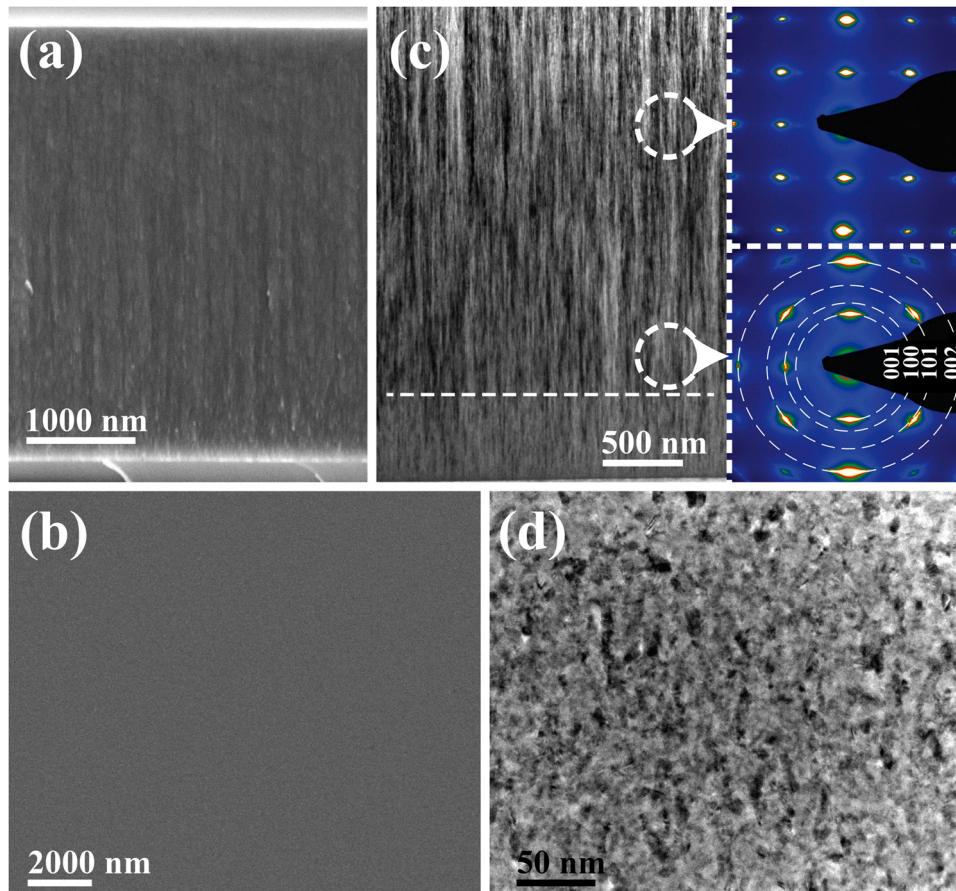


Fig. 1. Cross-sectional and plan-view (a and b) SEM and (c and d) bright-field TEM images of the as-deposited $TiB_{2.5}$ thin film. Insets in (c) show cross-sectional SAED patterns acquired from areas close to the substrate and the film's surface, indicated by dashed circles.

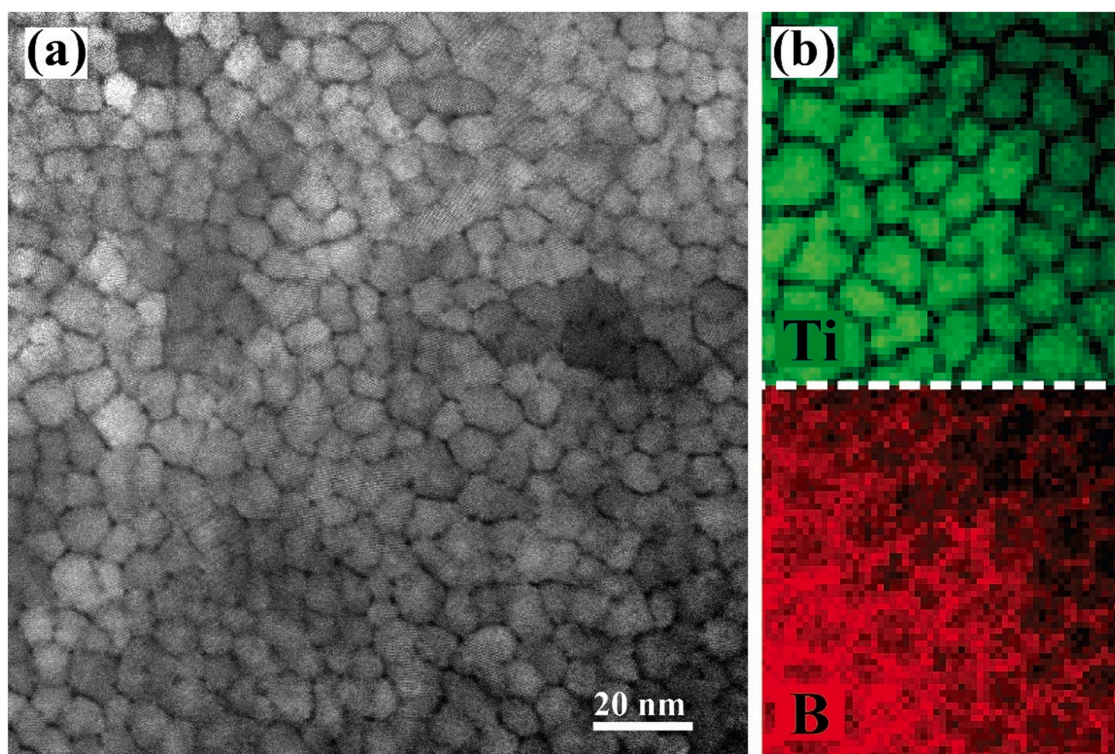


Fig. 2. Plan-view (a) HAADF-STEM micrograph and (b) Ti-L2,3 and B-K elemental distribution EELS maps of the as-deposited $\text{TiB}_{2.5}$ thin film acquired from an area close to the film's surface.

where E is the elastic modulus of the film determined by nano-indentation (420 ± 10 GPa), and α_s is the thermal expansion coefficient of Si substrate ($3.6 \times 10^{-6} \text{ K}^{-1}$ [60]). α_f and ν are the thermal expansion coefficient and the Poisson's ratio of the film; however, since they are unknown for $\text{TiB}_{2.5}$, we use the values of bulk TiB_2 ($7.0 \times 10^{-6} \text{ K}^{-1}$ for α_f and 0.11 for ν [61]). Thus, σ_{th} is estimated to be 0.76 ± 0.02 GPa. In spite of the significant difference between α_s and α_f , both cross-sectional and plan-view SEM and TEM results show a good adhesion between the substrate and film, with absolutely no crack in the 4000-nm-thick $\text{TiB}_{2.5}$, due possibly to the high diboride stiffness. The as-deposited $\text{TiB}_{2.5}$ thin film has a compressive residual stress of $\sigma_f = 1.1 \pm 0.2$ GPa and a hardness of 35 ± 2 GPa.

3.2. Composition and microstructure of air-annealed $\text{TiB}_{2.5}$

Fig. 3 shows the XSEM images of the $\text{TiB}_{2.5}$ thin films air-annealed at $T_a = 300, 400, 500, 600$, and 700°C up to $t_a = 48$ h. The oxide layers formed after air-annealing at $T_a = 300$ and 400°C have a columnar structure with columns that become thicker with increasing annealing time, Fig. 3(a) to 3(j). Their XSEM images also reveal that the scales resulting from air-annealing at 400°C have higher surface roughness than those formed at 300°C . Some deep cracks appear in the oxide scales formed at $T_a = 400^\circ\text{C}$ after air-annealing for $t_a \geq 24$ h, shown in Fig. 3(i) and 3(j). The oxide scales at $T_a = 500^\circ\text{C}$ are much thicker than those formed at $T_a = 300$ and 400°C . In addition, these scales show different morphologies; they have a highly porous structure with wide cracks formed through the scales for $t_a \geq 5$ h, see Fig. 3(k), 3(l), and 3(m). The entire $\text{TiB}_{2.5}$ film is oxidized for $t_a > 12$ h.

The cross-sectional morphology of the oxide layers changes drastically upon increasing annealing temperature to 600°C . At $T_a = 600^\circ\text{C}$, the oxide scales, which do not have any cracks, are composed of two layers; (i) an outer layer consisting of equiaxed crystallites and (ii) a dense inner layer, see Fig. 3(n) to 3(r). The average thickness of the outer layer does not significantly change as a function of t_a and is 170 ± 12 nm, while the thickness of the inner layer increases from 95

± 9 nm for $t_a = 1$ h to 374 ± 24 nm for $t_a = 48$ h. The oxide scales resulting from air-annealing at $T_a = 700^\circ\text{C}$ show an almost similar structure to those formed at $T_a = 600^\circ\text{C}$, in which a layer of loosely-attached sub-micrometer crystallites is visible on top of an inner layer, Fig. 3(s) to 3(v). However, the crystallites on top of these scales are larger than those formed after air-annealing at $T_a = 600^\circ\text{C}$. In addition, opposite to the columnar inner layer at $T_a = 600^\circ\text{C}$, the bottom layer formed after air-annealing at 700°C is highly porous and mostly composed of elongated large crystallites. The scales at $T_a = 700^\circ\text{C}$ also have deep cracks extended toward the oxide/film interfaces, not shown in Fig. 3(s) to 3(v).

To evaluate the influence of thermal history (heating-up duration from room temperature to T_a) on the morphology and thickness of the oxide scales, the $\text{TiB}_{2.5}$ thin films are air-annealed at $T_a = 600$ and 700°C for $t_a = 3$ h with two different lower heating rates ($\beta = 5.0$ and 1.0°C/min). The oxide scales formed using $\beta = 5.0^\circ\text{C/min}$ have similar cross-sectional morphologies and average thicknesses to those formed using $\beta = 10.0^\circ\text{C/min}$. However, air-annealing with $\beta = 1.0^\circ\text{C/min}$ results in the formation of oxide scales consisting of two different layers: an outer layer that appears similar to the one which forms at $T_a = 500^\circ\text{C}$, and an inner layer that is similar to the scale which forms at $T_a = 600/700^\circ\text{C}$ (depending on oxidizing temperature).

The effect of the thermal history is further studied by directly air-annealing $\text{TiB}_{2.5}$ at $T_a = 500, 600$, and 700°C . For each T_a , one as-deposited sample is placed into the furnace immediately after reaching the maximum annealing temperature and oxidized for $t_a = 3$ h (the samples do not experience the heating-up duration and are directly air-annealed at each T_a). The corresponding XSEM images in supplementary Fig. S1 exhibit similar oxide-scale morphologies to those shown in Fig. 3 (k), 3(n), and 3(s). The direct air-annealing also does not lead to a notable change in the average scale thickness. These results reveal that the oxide-scale growth and morphology at each T_a are not significantly influenced by the thermal history before reaching T_a for $\beta \geq 5.0^\circ\text{C/min}$.

Fig. 4 exhibits the plan-view SEM images of the $\text{TiB}_{2.5}$ thin films air-

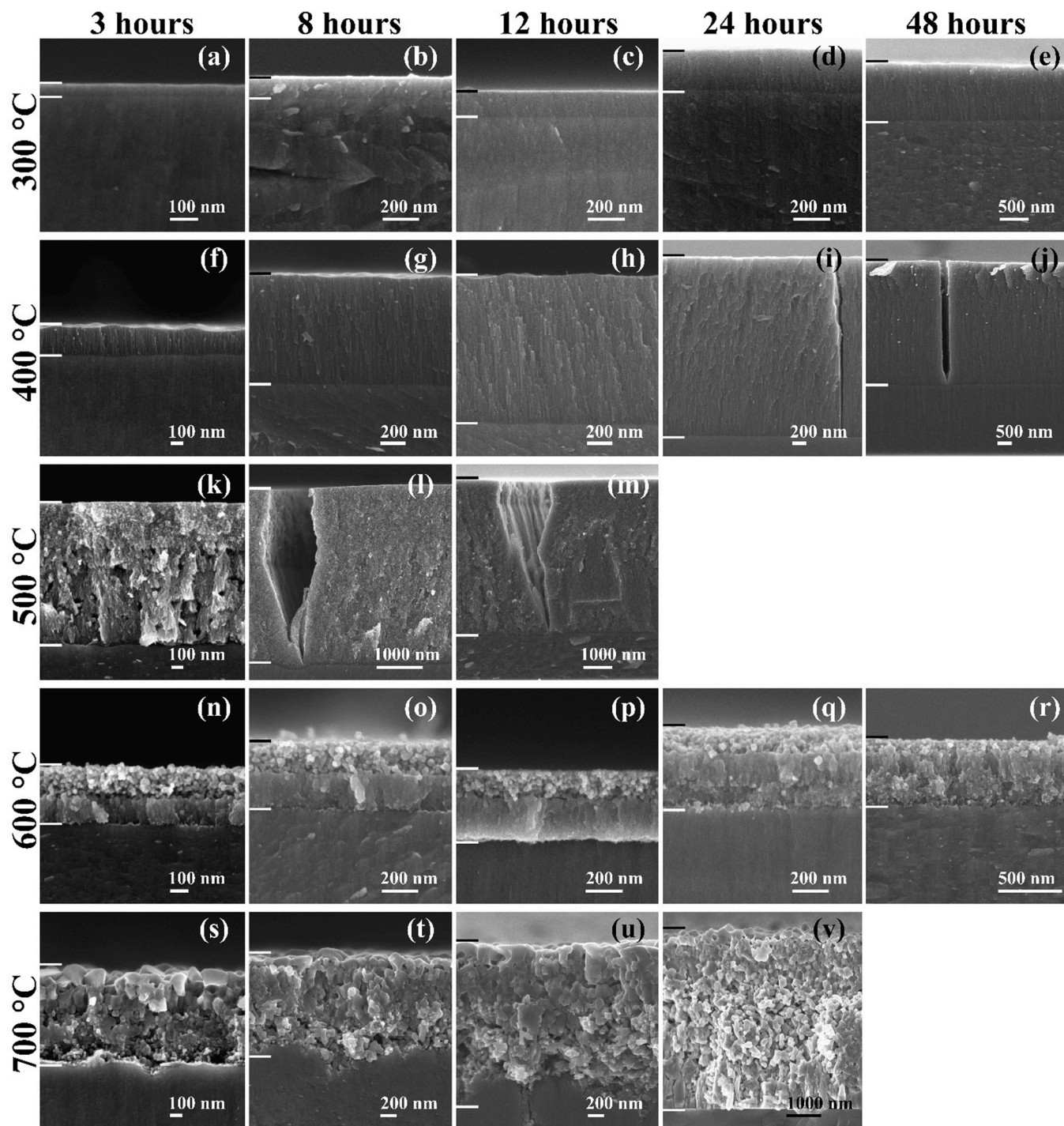


Fig. 3. Cross-sectional SEM images of $\text{TiB}_{2.5}$ air-annealed at $T_a = 300$ °C for (a) 3 h, (b) 8 h, (c) 12 h, (d) 24 h, and (e) 48 h; $T_a = 400$ °C for (f) 3 h, (g) 8 h, (h) 12 h, (i) 24 h, and (j) 48 h; $T_a = 500$ °C for (k) 3 h, (l) 8 h, and (m) 12 h; $T_a = 600$ °C for (n) 3 h, (o) 8 h, (p) 12 h, (q) 24 h, and (r) 48 h; and $T_a = 700$ °C for (s) 3 h, (t) 8 h, (u) 12 h, and (v) 24 h.

annealed at $T_a = 300, 400, 500, 600,$ and 700 °C up to $t_a = 48$ h. The oxide layers at $T_a = 300$ °C show smooth, featureless surfaces for $t_a \leq 24$ h, Fig. 4(a) to 4(d). However, for $t_a = 48$ h, the surface morphology, Fig. 4(e), becomes more similar to those of the oxide scales formed after air-annealing at 400 °C, Fig. 4(f) to 4(j), which appear like bright spots in a dark matrix. There are also some surface cracks formed after air-annealing at 400 °C for $t_a \geq 24$ h, see Fig. 4(i) and 4(j).

Air-annealing at $T_a = 500$ °C results in the oxide scales with surfaces that are highly porous and contain cracks, Fig. 4(k), 4(l), and 4(m). The width of these cracks significantly increases as a function of t_a . A plan-

view SEM image acquired at lower magnification, shown in [supplementary Fig. S2](#), exhibits a network of connected wide cracks in the layer air-annealed at 500 °C for $t_a = 12$ h. The surfaces of the oxide layers formed after air-annealing at $T_a = 600$ °C are composed of equiaxed crystallites that do not significantly change with increasing t_a , see Fig. 4 (n) to 4(r). No surface cracking is observed on these scales. Compared to $T_a = 600$ °C, the oxide scales on $\text{TiB}_{2.5}$ air-annealed at 700 °C, Fig. 4(s) to 4(v), show surfaces containing large crystallites and cracks. However, these cracks are not as wide as those formed after air-annealing at $T_a = 500$ °C.

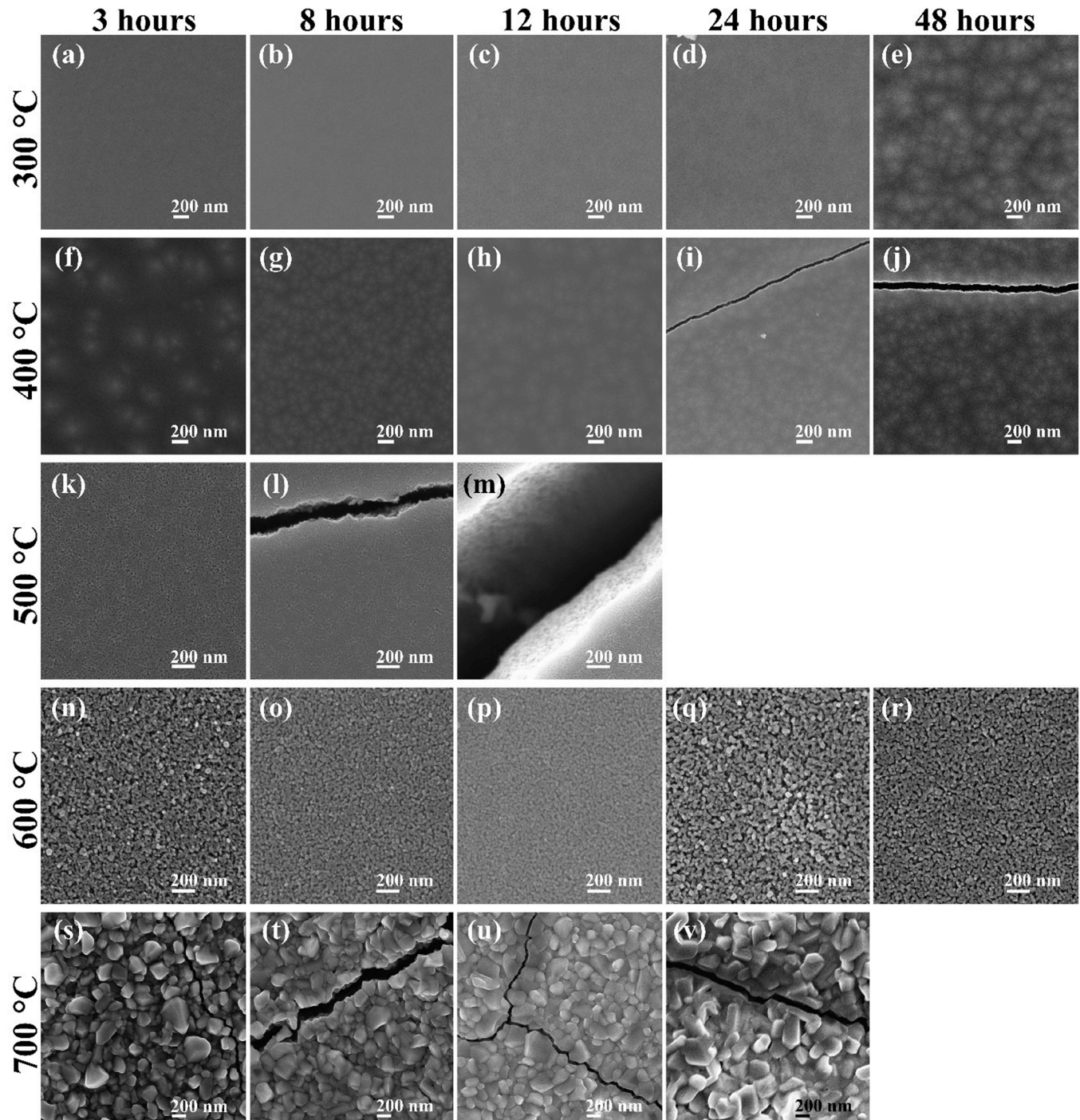


Fig. 4. Plan-view SEM images of $\text{TiB}_{2.5}$ air-annealed at $T_a = 300$ °C for (a) 3 h, (b) 8 h, (c) 12 h, (d) 24 h, and (e) 48 h; $T_a = 400$ °C for (f) 3 h, (g) 8 h, (h) 12 h, (i) 24 h, and (j) 48 h; $T_a = 500$ °C for (k) 3 h, (l) 8 h, and (m) 12 h; $T_a = 600$ °C for (n) 3 h, (o) 8 h, (p) 12 h, (q) 24 h, and (r) 48 h; and $T_a = 700$ °C for (s) 3 h, (t) 8 h, (u) 12 h, and (v) 24 h.

Fig. 5 compares the XRD θ - 2θ scans of as-deposited $\text{TiB}_{2.5}$ and the films air-annealed at $T_a = 300, 400, 500, 600,$ and 700 °C up to $t_a = 48$ h. The peaks at 32.8° are the (002) forbidden reflection arising from the Si(001) substrate, which appear due to multiple scattering events [62]. The XRD pattern of as-deposited $\text{TiB}_{2.5}$ contains (001), (101), and (002) peaks at $27.7^\circ, 44.5^\circ,$ and 57.2° , respectively. The (002) peak is not shown in Fig. 5. These reflections originate from a single diboride phase with the hexagonal crystal structure. The as-deposited film shows a strong (001) fiber texture, in which the (001) and (002) peaks are dominant, while the (101) peak is a minor

component.

Air-annealing the $\text{TiB}_{2.5}$ thin films at $T_a = 300$ and 400 °C does not result in the formation of new peaks in their XRD patterns, see Fig. 5(a) and 5(b), indicating that the formed oxide scales have X-rays amorphous crystal structures. There is also no notable change in peak positions up to $t_a = 48$ h. This shows that the levels of residual macro-strains in the films do not vary largely [63]. However, the (101) peak disappears after 12-h annealing. In addition, the full-width at half-maximum (FWHM) values of the (001) peaks decrease from $\sim 0.45^\circ$ for as-deposited $\text{TiB}_{2.5}$ to $\sim 0.34^\circ$ for the layer air-annealed at 400 °C for $t_a = 48$ h. This decrease

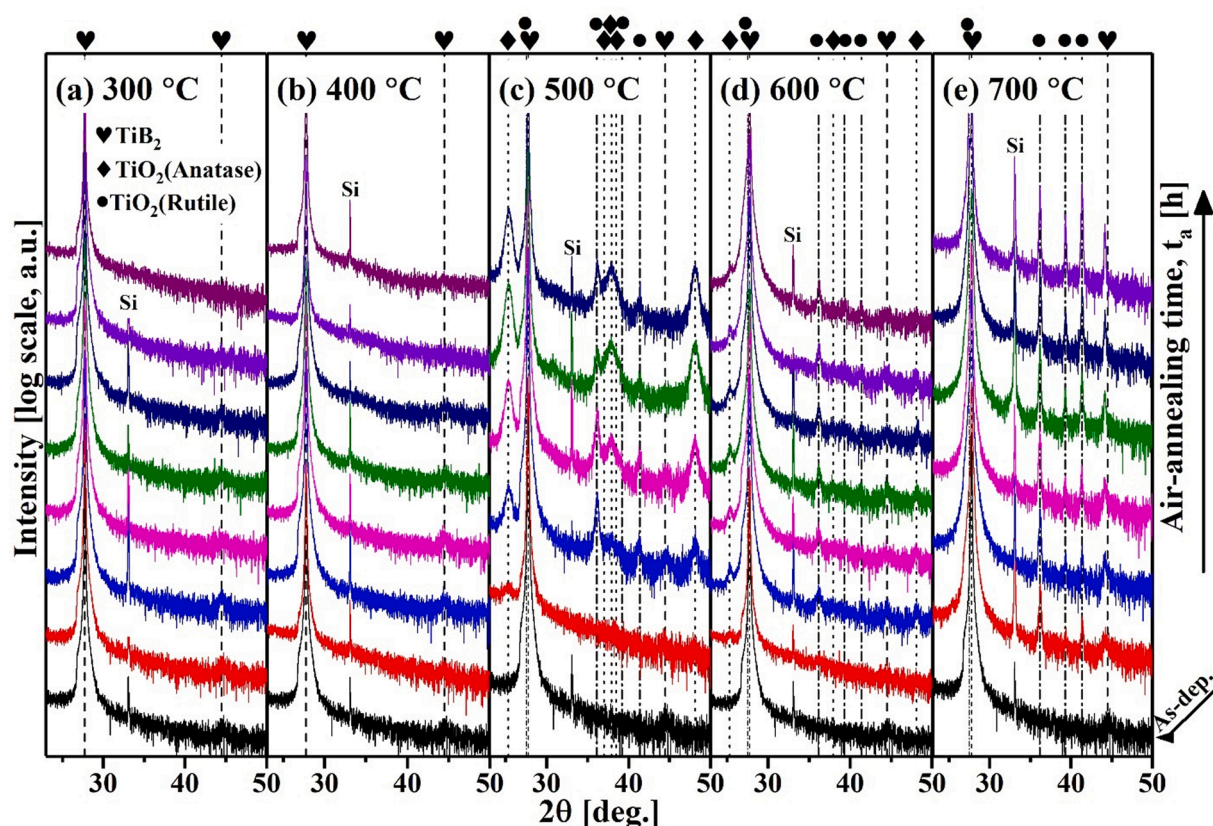


Fig. 5. XRD θ - 2θ scans of as-deposited $\text{TiB}_{2.5}$ and the films air-annealed at (a) $T_a = 300^\circ\text{C}$ for $t_a = 1, 3, 5, 8, 12, 24$, and 48 h, (b) $T_a = 400^\circ\text{C}$ for $t_a = 1, 3, 5, 8, 12, 24$, and 48 h, (c) $T_a = 500^\circ\text{C}$ for $t_a = 1, 3, 5, 8$, and 12 h, (d) $T_a = 600^\circ\text{C}$ for $t_a = 1, 3, 5, 8, 12, 24$, and 48 h, and (e) $T_a = 700^\circ\text{C}$ for $t_a = 1, 3, 5, 8, 12$, and 24 h. Vertical dashed (♥), dotted (♦), and dash-dotted (•) lines correspond to reference powder-diffraction peak positions for TiB_2 [73], anatase- TiO_2 [67], and rutile- TiO_2 [68], respectively. The peak at 32.8° is the (002) forbidden reflection arising from $\text{Si}(001)$ substrate [62].

cannot be due to an increase in domain sizes because the annealing temperatures ($\leq 400^\circ\text{C}$) are well below the temperature required for activating recrystallization and grain growth. Bulk diffusion that leads to recrystallization typically takes place at a homologous temperature T_h (annealing temperature to melting-point temperature ratio) above ~ 0.5 [64], while T_h is ~ 0.13 at 400°C . Instead, the decrease in the FWHM values at this T_a range is mostly attributed to a reduction in the levels of residual micro-strains in $\text{TiB}_{2.5}$ that occurs mainly by the annihilation of point defects such as vacancies, interstitials, and anti-site substitutions of atoms, which usually have significant fractions in sputter-deposited coatings [19,65]. The point-defect annihilation requires considerably lower activation energies than recrystallization [66].

At $T_a \geq 500^\circ\text{C}$, in addition to the peaks arising from the diboride phase, new reflections appear in the XRD patterns of air-annealed $\text{TiB}_{2.5}$, Fig. 5(c), 5(d), and 5(e), which can be assigned to anatase- TiO_2 [67] and rutile- TiO_2 [68] phases with tetragonal crystal structures. At $T_a = 500^\circ\text{C}$, the oxide-phase XRD reflections originate from both anatase and rutile, but the dominant peaks are from the anatase phase, see Fig. 5(c). The intensities of these peaks increase as a function of t_a due mainly to an increase in the volume and crystallinity of the anatase phase. In addition, their FWHM values also increase due possibly to a decrease in the grain sizes. The oxide-phase peaks in the XRD patterns of the layers air-annealed at $T_a = 600^\circ\text{C}$ do not have high intensities due to the formation of oxide scales that are thin and show the presence of both anatase and rutile phases. There is also no notable change in the peak intensities as a function of t_a . In contrast, the oxide-phase peaks in the XRD patterns of $\text{TiB}_{2.5}$ air-annealed at $T_a = 700^\circ\text{C}$ arise just from the rutile- TiO_2 phase, where the peak intensities increase with increasing t_a , see Fig. 5(e). This is consistent with the transformation of bulk anatase to rutile that occurs at $\sim 600^\circ\text{C}$ in air [69–71] and is not instantaneous

as it is reconstructive [72]. For both $T_a = 500$ and 700°C , the intensities of the diboride peaks decrease as a function of t_a due to the evolution of the oxide phase during the air-annealing process.

XPS core-level spectra from the $\text{TiB}_{2.5}$ thin films air-annealed at $T_a = 300^\circ\text{C}$ for $t_a = 12$ h and $T_a = 400, 500, 600$, and 700°C for $t_a = 3$ h are acquired in order to evaluate the chemistry of the oxidation products. For $T_a = 300^\circ\text{C}$, the sample air-annealed for $t_a = 12$ h is chosen for XPS and TEM studies because it has a thicker oxidation product compared to the $t_a = 3$ h case. Fig. 6 compares the Ti, B, and O core-level spectra obtained at sputtering depth $d_{\text{sput}} = \sim 65$ nm. The Ti 2p spectra in Fig. 6(a) exhibit broad, convoluted signals consisting of several spin-split $2p_{3/2}$ - $2p_{1/2}$ doublets. The strongest $2p_{3/2}$ signals at ~ 459.5 eV are assigned to Ti atoms in TiO_2 . In addition, there is evidence for several substoichiometric oxides denoted as TiO_Δ ($\Delta = \text{O}/\text{Ti} < 2$), with the $2p_{3/2}$ peaks in the range 455.0 – 458.5 eV, which are the artefacts of Ar^+ sputter etching [74]. The intensity of the $2p_{3/2}$ signals from the TiO_Δ phase appeared at ~ 458.5 eV decreases with increasing T_a , while it significantly increases for the TiO_2 phase (signals at ~ 459.5 eV). The $2p_{3/2}$ signal position corresponding to the Ti-B bonds of the TiB_2 phase, ~ 454.7 eV, is also indicated in Fig. 6(a). However, based on the B 1s spectra discussed below, we infer that Ti-B is only present for $T_a = 300$ and 400°C . The B 1s spectra acquired from the $\text{TiB}_{2.5}$ thin films air-annealed at $T_a = 300, 400$, and 500°C , Fig. 6(b), comprise two signals centered at ~ 193.0 eV, which can be assigned to B in B-O, and ~ 188.0 eV, indicative of B in Ti-B. Markedly, the B 1s signal in the spectrum of the layer air-annealed at 500°C is very weak (see also XPS and ToF-ERDA depth-profile results in Fig. 7(c) and 8(a)), while no B signal is detected in the B 1s spectra from the films air-annealed at $T_a = 600$ and 700°C . The O 1s spectra in Fig. 6(c) are composed of convoluted signals mainly arising from TiO_2 , TiO_Δ , and B-O for $T_a < 500^\circ\text{C}$

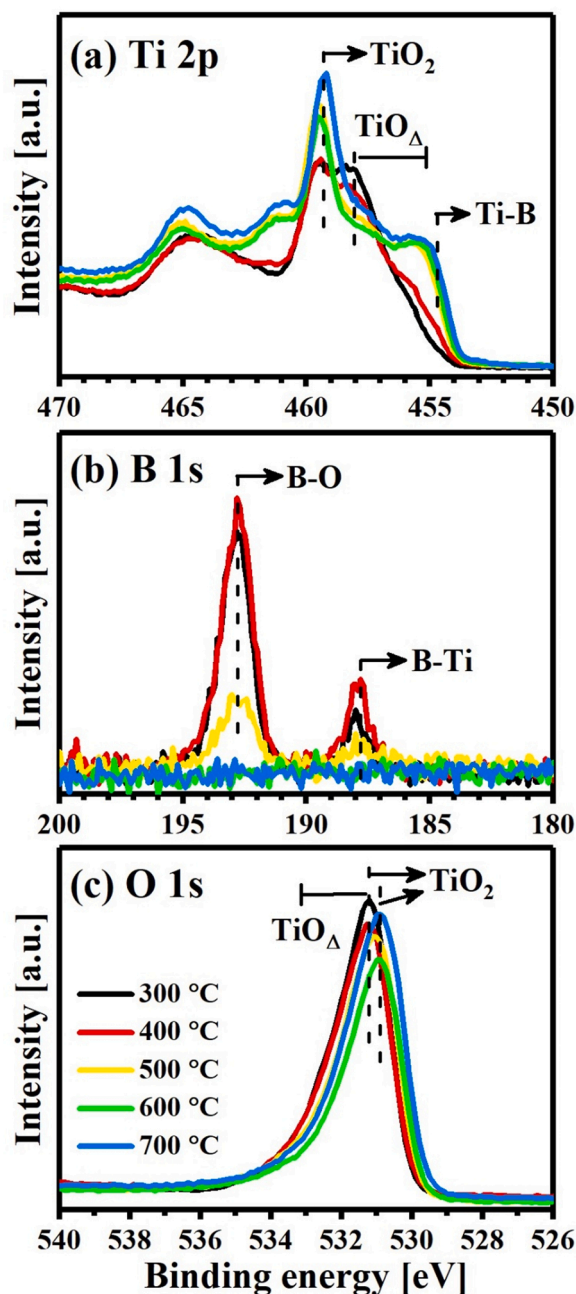


Fig. 6. (a) Ti 2p, (b) B 1s, and (c) O 1s XPS core-level spectra acquired from the $\text{TiB}_{2.5}$ thin films air-annealed at $T_a = 300$ °C for $t_a = 12$ h and $T_a = 400$, 500, 600, and 700 °C for $t_a = 3$ h at sputtering depth $d_{\text{sput}} = \sim 65$ nm.

and TiO_2 and TiO_Δ for $T_a \geq 500$ °C, in agreement with the Ti 2p and B 1s signals. These peaks have almost similar shapes for all T_a . The O 1s signals for $\text{TiB}_{2.5}$ air-annealed at $T_a = 300$ and 400 °C appear shifted by ca. 0.4 eV to lower binding energy with respect to those from the films annealed at $T_a \geq 500$ °C. Such small shifts in the oxide layers are difficult to interpret as they can likely result from varying charging conditions. The evolutions of B, O, and Ti core-level spectra as a function of sputtering depth d_{sput} are plotted in [supplementary Fig. S3](#).

XPS depth profiles reconstructed from the raw spectra of the $\text{TiB}_{2.5}$ thin films air-annealed at $T_a = 300$ °C for $t_a = 12$ h and $T_a = 400$, 500, 600, and 700 °C for $t_a = 3$ h are shown in [Fig. 7](#). The XPS chemical compositions are normalized to corresponding concentrations determined from ToF-ERDA measurements in order to minimize the influence of preferential sputtering effects, which cannot be completely avoided

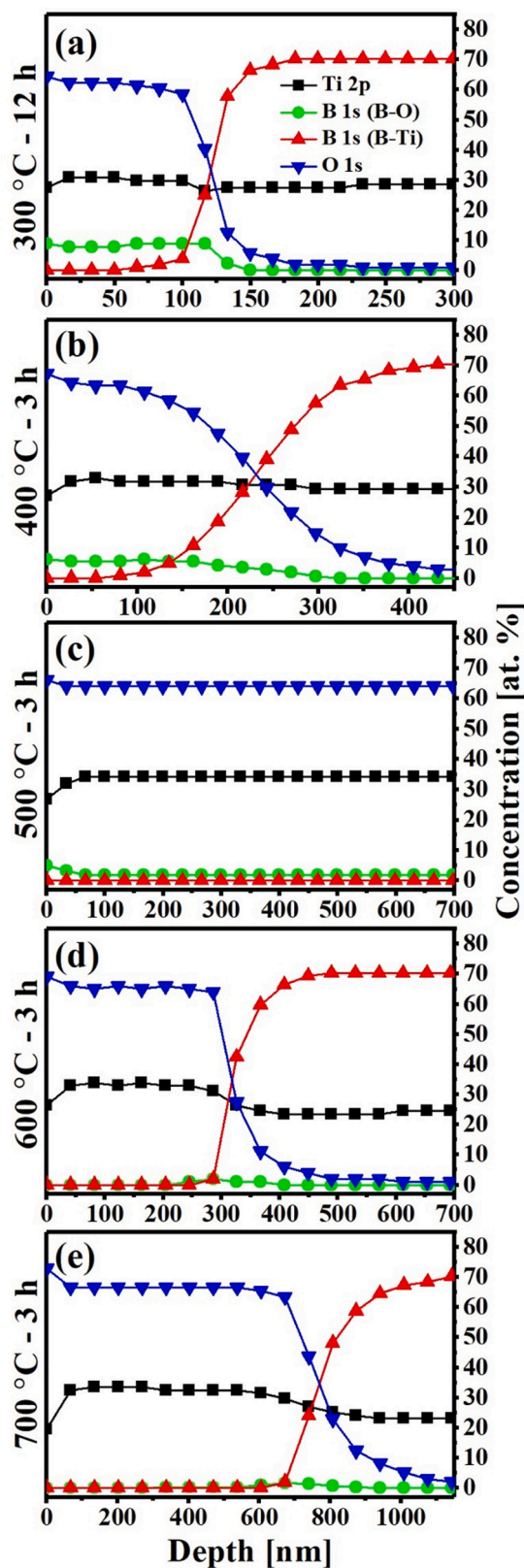


Fig. 7. XPS elemental concentration depth profiles of the $\text{TiB}_{2.5}$ thin films air-annealed at (a) 300 °C for $t_a = 12$ h, (b) 400, (c) 500, (d) 600, and (e) 700 °C for $t_a = 3$ h as a function of the sputtering depth d_{sput} . The XPS compositions are normalized to corresponding values determined from ToF-ERDA measurements.

during depth profiling with Ar^+ ions [54,75]. All depth profiles in Fig. 7 show uniform elemental distributions within the oxide layers. The depth profiles in Fig. 7(a) and 7(b) reveal that the oxide scales formed after air-annealing at $T_a = 300$ and 400°C contain ~ 8 and ~ 6 at% B, respectively, in the oxide (B-O) phase, while the scales do not have B in the diboride (B-Ti) phase. The XPS result of $\text{TiB}_{2.5}$ air-annealed at $T_a = 500^\circ\text{C}$ reveals that the oxide layer contains < 2 at% B in the oxide phase, see Fig. 7(c). Contrary to $T_a \leq 500^\circ\text{C}$, the scales formed after air-annealing at $T_a = 600$ and 700°C are highly B-deficient, Fig. 7(d) and 7(e).

The elemental distributions within oxide scales of all air-annealed $\text{TiB}_{2.5}$ thin films are further investigated by means of ToF-ERDA depth profiles (not shown). In agreement with the XPS results, the ToF-ERDA depth profiles reveal uniform elemental depth distributions within all oxide layers. This confirms that the chemistry of the oxidation products formed on the $\text{TiB}_{2.5}$ thin films does not change along the scale thicknesses for all T_a ranging from 300° to 700°C .

The average B, O, and Ti concentrations, determined from the ToF-ERDA depth profiles, in the oxide scales formed after air-annealing at $T_a = 300, 400, 500, 600$, and 700°C are plotted as a function of t_a in Fig. 8. For $T_a = 300$ and 400°C , after excluding the concentrations of $t_a = 3$ and 5 h – as their corresponding oxide layers are very thin causing large uncertainties, the B concentrations remain almost constant, while the O and Ti concentrations change with increasing t_a . The average B content is 8.1 ± 0.6 at% and 7.0 ± 0.5 at% in the oxidation products formed after air-annealing at 300 and 400°C , respectively. At $T_a = 300^\circ\text{C}$, the average O concentration increases from 62.1 ± 1.3 at% for $t_a = 8$ h to 66.1 ± 0.7 at% for $t_a = 48$ h, while the average Ti content decreases from 29.6 ± 0.8 at% to 25.1 ± 0.6 at%. This results in the O/Ti ratios ranging from ~ 2.1 for $t_a = 8$ h to ~ 2.6 for $t_a = 48$ h. At $T_a = 400^\circ\text{C}$, the O concentration changes from 65.6 ± 0.4 at% to 67.8 ± 0.5 at%, and the average Ti content decreases from 27.5 ± 0.6 at% to 24.7 ± 0.5 at% as a function of t_a , representing an increase in the O/Ti ratio from ~ 2.4 to ~ 2.7 .

For $T_a \geq 500^\circ\text{C}$, the oxidation products are highly B-deficient. The average B concentrations are 1.1 ± 0.2 at%, 0.4 ± 0.1 at%, and 0.2 ± 0.1 at% in the scales formed after air-annealing at $500, 600$, and 700°C , respectively. In contrast to $T_a = 300$ and 400°C , the average O and Ti content does not change significantly with increasing t_a for $T_a \geq 500^\circ\text{C}$. The O concentrations are 64.5 ± 0.5 at%, 66.0 ± 0.3 at%, and 67.0 ± 0.3 at% in the oxide layers formed after air-annealing at $T_a = 500, 600$, and 700°C , respectively, while the Ti concentrations are 34.1 ± 0.2 at%, 33.0 ± 0.2 at%, and 33.0 ± 0.5 at%, respectively; indicating a TiO_2 chemistry.

Fig. 9 comprises the HAADF-XSTEM micrographs together with SAED patterns and EELS elemental maps of the $\text{TiB}_{2.5}$ thin films air-annealed at $T_a = 300^\circ\text{C}$ for $t_a = 12$ h and $T_a = 400, 500, 600$, and 700°C for $t_a = 3$ h. The SAED patterns are obtained from two regions indicated by * and * symbols in the HAADF-XSTEM micrographs; one close to the surface of the oxide scales (*) and one near the oxide/film interfaces (*). Prior to ion milling in FIB, the targeted areas on the specimens are protected by depositing Pt, which appears bright on top of the oxidation products in the HAADF-XSTEM micrographs in Fig. 9. In addition, some bright Pt particles can be also observed (mostly at porous regions) that are unavoidable artifacts coming from redistribution of the top Pt layer during the final steps of specimen thinning process.

The oxide layer formed after air-annealing at $T_a = 300^\circ\text{C}$, 100 ± 7 nm thick, exhibits a cross-sectional nanostructure with some porosity, Fig. 9(a) and supplementary Fig. S4. The B-K, O-K, and Ti-L_{2,3} EELS maps show that the scale is mainly composed of uniformly distributed O and Ti with weak B signals. Air-annealing $\text{TiB}_{2.5}$ at $T_a = 400^\circ\text{C}$ for $t_a = 3$ h results in the formation of an oxidation product with a thickness of 193 ± 10 nm that has a nanostructure resembling vertically aligned fibers with porosity extending along their boundaries in the [001] direction, Fig. 9(b). The EELS maps exhibit weak B signals and some discontinuities between the Ti signals. The O-K EELS map,

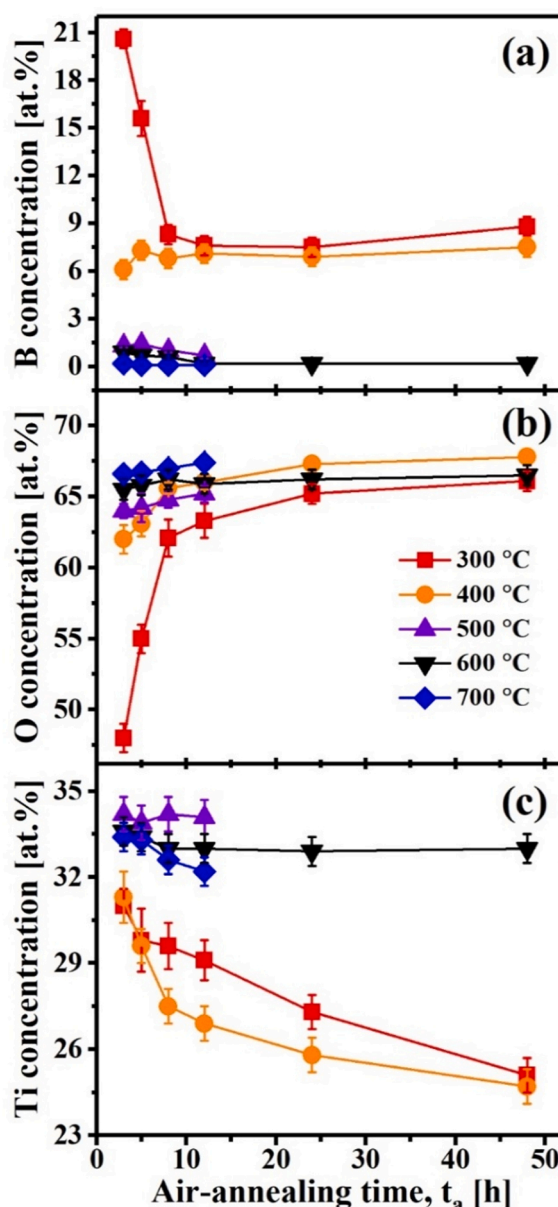


Fig. 8. Average B, O, and Ti concentrations, obtained from the ToF-ERDA depth profiles, in the oxide scales formed on the $\text{TiB}_{2.5}$ thin films after air-annealing at $T_a = 300, 400, 500, 600$, and 700°C as a function of t_a .

however, shows a uniform distribution for oxygen. The SAED patterns of the scales formed after air-annealing at $T_a = 300$ and 400°C consist of wide, diffuse rings revealing that the oxide phases are amorphous, corroborating the XRD results in Fig. 5.

Contrary to $T_a = 300$ and 400°C , the HAADF-XSTEM micrograph of the $\text{TiB}_{2.5}$ thin film air-annealed at $T_a = 500^\circ\text{C}$ for $t_a = 3$ h, Fig. 9(c), indicates a thick oxide scale that consists of two layers. The top porous layer with a thickness of 310 ± 20 nm is composed of nodular grains, and the inner layer that is 780 ± 15 nm thick contains porosity and large voids. The B-K EELS map in Fig. 9(c) proves the XPS and ToF-ERDA results in Figs. 7 and 8 that the oxidation product formed after air-annealing at $T_a = 500^\circ\text{C}$ is highly B-deficient. The O-K and Ti-L_{2,3} EELS maps also confirm the presence of large voids in the inner layer. The voids are that large that they do not contain even much O; instead, they are C-rich, coming from TEM specimen preparation and air exposure, see supplementary Fig. S5.

The oxide scale formed after air-annealing at $T_a = 600^\circ\text{C}$ and t_a

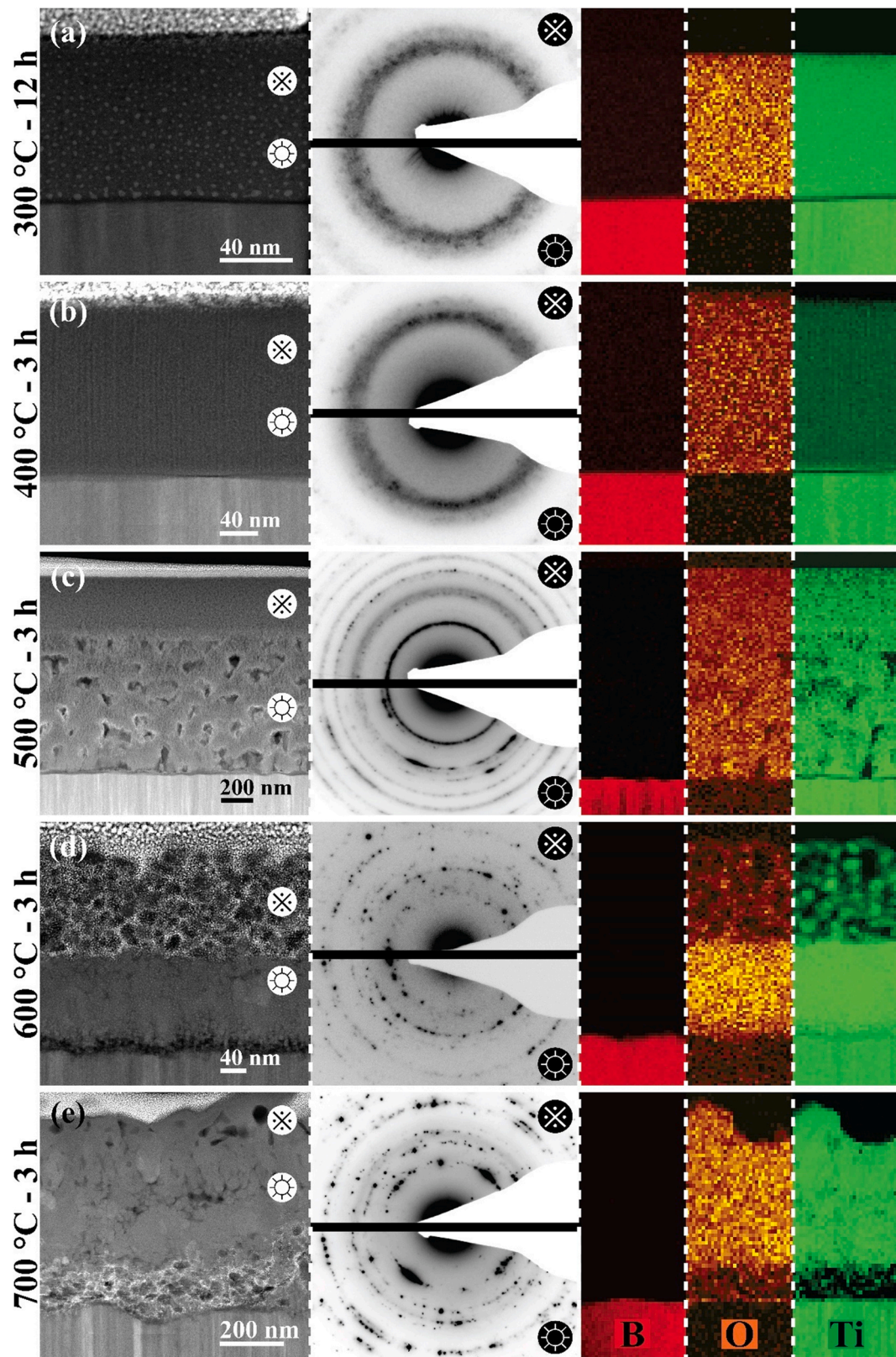


Fig. 9. Cross-sectional HAADF-STEM micrographs together with SAED patterns and B-K, O-K, and Ti-L2,3 EELS maps of the $\text{TiB}_{2.5}$ thin films air-annealed at (a) 300 °C for $t_a = 12$ h, (b) 400, (c) 500, (d) 600, and (e) 700 °C for $t_a = 3$ h. A layer of Pt is deposited on top of each oxide scale, appeared bright in the HAADF-STEM micrographs. The bright areas in the micrographs are Pt particles, unavoidable artifacts coming from TEM specimen preparation. The regions indicated by \otimes and \odot symbols exhibit the areas where the SAED patterns as well as plan-view HAADF-STEM micrographs and EELS elemental maps, shown in Fig. 11, are acquired from.

= 3 h, shown in Fig. 9(d), comprises two regions; an outer layer with a thickness of 140 ± 10 nm that is composed of equiaxed crystallites decorated by bright Pt particles and an inner layer with a thickness of 170 ± 12 nm that consists of two sublayers. The sublayer close to the oxide/film interface, 105 ± 5 nm thick, has grains extended along the [001] direction, while the sublayer near the equiaxed crystallites, 65 ± 4 nm thick, is mostly composed of small grains with almost round shapes and some porosity at grain boundaries. The B-K EELS map in Fig. 9(d) confirms that this oxide scale does not contain B. The O-K and Ti-L_{2,3} EELS maps prove that there are large voids between the equiaxed crystallites in the outer layer, while O and Ti are uniformly distributed in the inner layer.

The HAADF-XSTEM micrograph in Fig. 9(e) shows the oxide scale on TiB_{2.5} air-annealed at $T_a = 700$ °C for $t_a = 3$ h has two main regions. This scale has a top layer consisting of loosely-attached sub-micrometer crystallites that seem similar to those formed after air-annealing at 600 °C; however, these crystallites undergo significant coarsening. The inner layer is composed of grains that change in shape and sizes toward the oxide/film interface. The grains below the loosely-attached crystallites are elongated and show porosity at their interfaces, while the grains below this layer have irregular shapes and appear more packed. There are large voids, with accumulations of Pt particles coming from the TEM specimen preparation, at the oxide/film interface. Similar to $T_a = 600$ °C, no B signal is detected in the EELS results from this scale. Both O-K and Ti-L_{2,3} EELS maps obviously show the oxide/film interface is highly porous. The SAED patterns of the scales formed after air-annealing at 500, 600, and 700 °C have diffraction components indicating that these layers are composed of crystalline phases.

Fig. 10 shows the XTEM micrographs acquired from the inner layer of the oxide scale formed after air-annealing at $T_a = 600$ °C and $t_a = 3$ h. The micrograph in Fig. 10(a) indicates that the bottom sublayer, which is close to the oxide/film interface, consists of columnar TiO₂ grains with no detectable porosity along their grain boundaries. The formation of these dense grain boundaries is also proved by high-resolution XTEM

(HR-XTEM) micrographs, not shown here. The HR-XTEM micrographs acquired from an area between the sublayers, the interface between the bottom sublayer (columnar grains) and the top sublayer (small grains with almost round shapes), shown in Fig. 10(b) and 10(c), reveal the presence of an amorphous phase. To confirm the formation of such amorphous structure, fast Fourier transform (FFT) analyses are performed on the HR-XTEM micrographs to determine the crystal structure in the reciprocal space. The FFT patterns from A boxes consist of diffraction spots proving crystalline structure, while the FFT patterns from the amorphous regions, B boxes, are composed of halo features demonstrating that these regions have amorphous structure.

Fig. 11 compares the plan-view HAADF-STEM micrographs and EELS elemental maps of the oxidation products formed on the TiB_{2.5} thin films air-annealed at $T_a = 300$ °C for $t_a = 12$ h and $T_a = 400, 500, 600$, and 700 °C for $t_a = 3$ h. These data are acquired from the regions indicated by * and * symbols in the HAADF-XSTEM micrographs shown in Fig. 9. B-K EELS maps for $T_a = 500, 600$, and 700 °C are not included in Fig. 11 since the corresponding spectra do not contain any detectable B signals. The oxide scales formed after air-annealing at $T_a = 300$ and 400 °C show plan-view nanostructures that do not significantly change along the scale thickness, see Fig. 11(a) to 11(d). Air-annealing at $T_a = 300$ °C results in a change in the plan-view grain shapes and formation of porosity, see Figs. 2, 11(a), 11(b), and supplementary Fig. S4. The EELS maps in Fig. 11(a) and 11(b) show almost uniform B, O, and Ti distributions. The plan-view HAADF-STEM micrographs in Fig. 11(c) and 11(d) exhibit that the vertically aligned fibers formed after air-annealing at $T_a = 400$ °C typically have round edges with a width of 6 ± 2 nm that their sizes do not noticeably change along the scale thickness. The EELS maps in Fig. 11(c) and 11(d) show that the dark regions, which appear between the fibers and become slightly larger toward the oxide-scale surface, are highly B-, O-, and Ti-deficient, while they are C-rich, see supplementary Fig. S5. This indicates that there are open areas formed in the nanostructure of the oxide scales.

In contrast to $T_a = 300$ and 400 °C, the plan-view HAADF-STEM

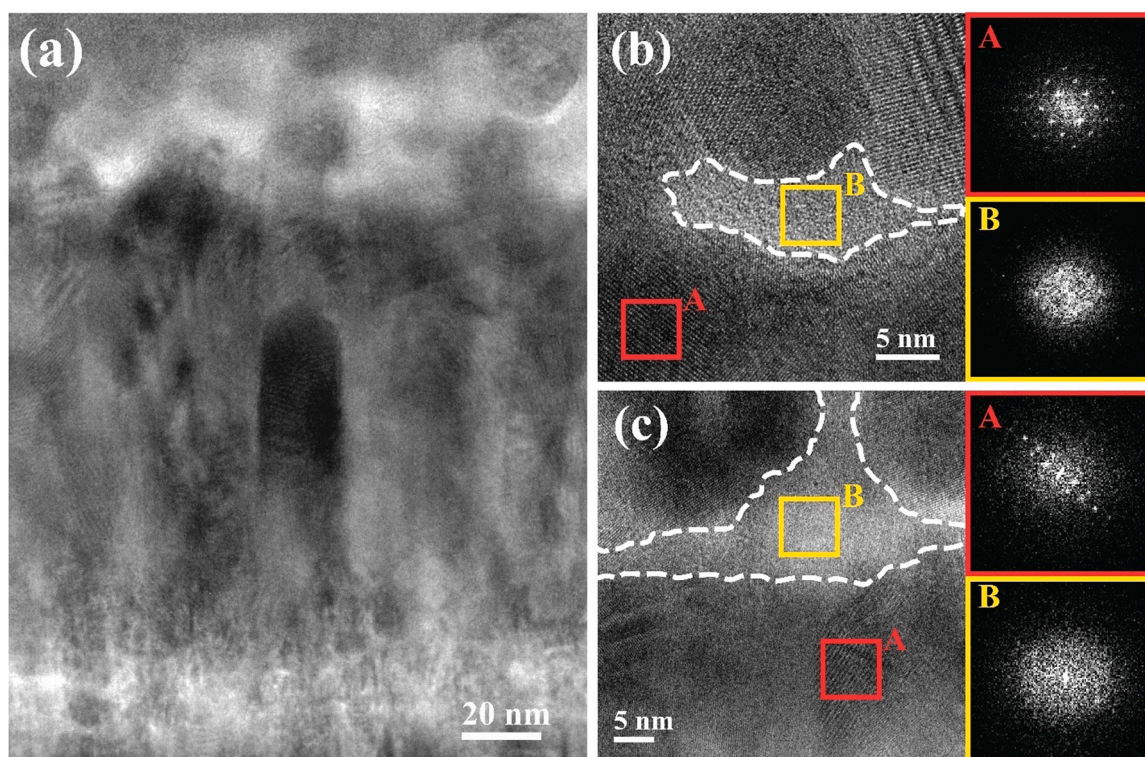


Fig. 10. (a) Cross-sectional TEM micrograph acquired from the inner layer of the oxide scale on the TiB_{2.5} thin film formed after air-annealing at $T_a = 600$ °C and $t_a = 3$ h, and (b and c) HR-XTEM micrographs from an area at the interface between top and bottom sublayers. Insets in (b) and (c) show FFT micrographs from regions indicated by A and B boxes.

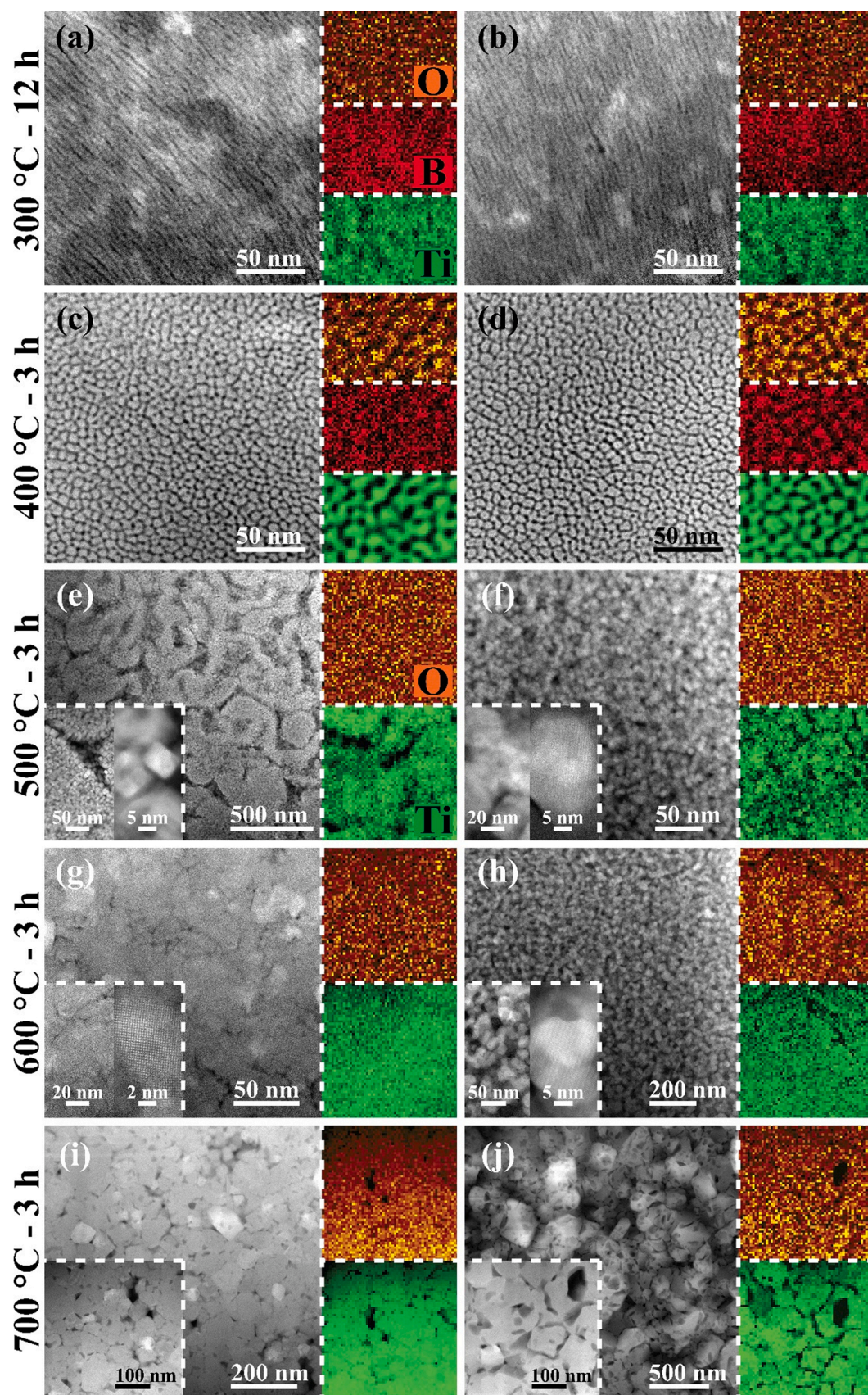


Fig. 11. Plan-view HAADF-STEM micrographs together with the EELS maps of the $\text{TiB}_{2.5}$ thin films air-annealed at (a and b) 300 °C for $t_a = 12$ h, (c and d) 400, (e and f) 500, (g and h) 600, and (i and j) 700 °C for $t_a = 3$ h. The plan-view HAADF-STEM micrographs and EELS elemental maps are acquired from the regions indicated by * and * symbols in Fig. 9.

micrographs in Fig. 11(e) to 11(j) show notable changes in the nanostructures of TiB_{2.5} air-annealed at $T_a \geq 500$ °C. The region in the inner oxide scale formed after air-annealing at $T_a = 500$ °C, see Fig. 9(c), exhibits a nanostructure that is mainly composed of cubic crystallites with a size of 9 ± 2 nm, Fig. 11(e). In addition, it contains a high density of porosity and large voids (70 ± 25 nm), which is also confirmed by the O-K and Ti-L_{2,3} EELS maps shown in Fig. 11(e). The plan-view HAADF-STEM micrograph acquired from the top layer of the oxidation product formed after air-annealing at 500 °C, Fig. 9(c), indicates the presence of nodular grains with a diameter of 17 ± 6 nm, Fig. 11(f).

At $T_a = 600$ °C, the plan-view HAADF-STEM micrograph acquired from the outer layer of the oxide scale, see Fig. 9(d), is composed of equiaxed crystallites with a diameter of 16 ± 5 nm, Fig. 11(h). However, the micrograph acquired from the sublayer below the equiaxed crystallites has small grains with some porosity at grain boundaries, Fig. 11(g). Compared to the O-K and Ti-L_{2,3} EELS maps from the outer layer, Fig. 11(h), the maps from the sublayer near the equiaxed crystallites shown in Fig. 11(g) reveal more uniform distribution of O and Ti. The plan-view HAADF-STEM micrograph of TiB_{2.5} air-annealed at $T_a = 700$ °C shows that the loosely-attached crystallites in the outer layer, Fig. 9(e), have irregular shapes with a size of 185 ± 55 nm, see Fig. 11(j), while the oxide layer underneath the loosely-attached crystallites has grains (44 ± 16 nm) with sharp edges and large voids (37 ± 20 nm), Fig. 11(i). The O-K and Ti-L_{2,3} EELS maps in Fig. 11(i) and 11(j) also affirm the existence of large gaps and voids.

3.3. Oxidation kinetics of air-annealed TiB_{2.5}

Fig. 12 shows the XSEM-obtained thicknesses of oxide scales d_{ox} formed on the TiB_{2.5} thin films after air-annealing at $T_a = 300, 400, 500, 600$, and 700 °C up to $t_a = 120$ h. Over the entire t_a range, the oxide scales that grow on the layers air-annealed at 400 °C are thicker than those on the layers air-annealed at 300 °C. The TiB_{2.5} thin films exhibit abnormal oxidation behavior at $T_a = 500$ and 600 °C. Air-annealing at $T_a = 500$ °C results in the formation of oxide scales that are significantly thicker than the scales formed at the other T_a temperatures (even $T_a = 700$ °C), while the scales on the layers air-annealed at $T_a = 600$ °C are thinner than those formed after air-annealing at $T_a = 400$ °C. After $t_a = \sim 30$ h, air-annealing at $T_a = 600$ °C leads to the formation of oxide scales that are even thinner than the scales formed after air-annealing at

$T_a = 300$ °C.

The TiB_{2.5} thin films follow unprotective linear oxidation kinetics at $T_a = 300, 400, 500$, and 700 °C according to:

$$d_{ox} = a + k \cdot t_a, \quad (3)$$

where k is the oxidation-rate constant. The oxide growth rate significantly increases from $k = 10$ nm/h for $T_a = 300$ °C to $k = 88$ nm/h for $T_a = 400$ °C to $k = 442$ nm/h for $T_a = 500$ °C, while it decreases to $k = 179$ nm/h for $T_a = 700$ °C. In contrast, at $T_a = 600$ °C, the oxide scale does not grow linearly as a function of t_a and instead, it shows the following relationship:

$$d_{ox} = k \cdot t_a^n, \quad (4)$$

where $k = 250$ nm/h and $n = 0.2$. The oxidation rate at 600 °C becomes more stable after $t_a = 3$ h, see inset in Fig. 12, which reveals a protective oxidation behavior. The experimental data in Fig. 12 are fitted with including $t_a = 0$ h data point. To evaluate the accuracy of the oxidation rates, we also fit these experimental data without considering $t_a = 0$ h. The maximum deviation in the reported oxidation rates, with and without including $t_a = 0$ h data point in fitting, is achieved for $T_a = 300$ °C, which is $\sim 1\%$. This proves that the initial oxidation stage does not have a significant influence on the overall oxidation rates of TiB_{2.5} thin films.

The oxidation kinetics of the TiB_{2.5} thin films are further studied using a combination of thermogravimetric (TG) and differential scanning calorimetry (DSC) analyses. Fig. 13(a) and 13(b) compare the TG and DSC curves of the TiB_{2.5} powders acquired from the dynamic air-annealing measurements carried out with heating rates β of 1.0, 2.5, 5.0, 10.0, and 20.0 °C/min under a linear temperature programming up to 1000 °C. Oxidation parameters obtained from the TG and DSC curves are summarized in Table 1. The instantaneous weight of the powders is recorded, and the corresponding weight change α (also known as the degree of oxidation conversion) is simultaneously calculated according to the following equation [76]:

$$\alpha = [(W_i - W_t)/(W_i - W_f)] \times 100, \quad (5)$$

where W_i , W_t , and W_f are the initial, instantaneous, and final weights of the powders, respectively.

All TG curves in Fig. 13(a) exhibit a similar weight gain trend with different rates. The total weight gain from 200° to 1000° C increases from $\alpha = 21.5\%$ for $\beta = 20.0$ °C/min to $\alpha = 56.8\%$ for $\beta = 1.0$ °C/min, showing that the oxidation reaction rate for the TiB_{2.5} thin films depends on the heating rate. The curves comprise two main parts. For all β values, there is no significant weight change up to 455 ± 19 °C. The first significant weight gain starts from 455 ± 19 °C, which denotes the oxidation onset temperature T_{onset} , to 578 ± 16 °C is $\alpha = 5.1 \pm 0.5\%$. The further increase in the oxidation temperature from 578 ± 16 – 662 ± 13 °C does not lead to a considerable weight change, which is in agreement with the results for the TiB_{2.5} thin films air-annealed at $T_a = 600$ °C in Fig. 12. The second significant weight gain ($\alpha = 44.8 \pm 6.2\%$) takes place from 662 ± 13 – 911 ± 29 °C, indicating oxidation with a more rapid rate. The first derivative of the TG curve acquired with $\beta = 2.5$ °C/min is plotted in Fig. 13(c) to exemplify the noticeable weight changes and critical points.

The DSC results of the TiB_{2.5} powders determined at different β , shown in Fig. 13(b), exhibit two sets of convoluted exothermic signals that are accompanied by two significant weight gain events, see Fig. 13(c). These convoluted signals reveal that TiB_{2.5} undergoes complex oxidation processes. The first set consists of signals centered at $T_1 = 481 \pm 13$ °C, $T_2 = 500 \pm 9$ °C, and $T_3 = 540 \pm 4$ °C, with a total formation enthalpy ΔH_f of 1.60 ± 0.45 kJ/g. The second set has signals appeared at $T_1 = 766 \pm 10$ °C and $T_2 = 813 \pm 10$ °C, with $\Delta H_f = 2.15 \pm 0.46$ kJ/g.

As a reference, the TG and DSC data of stoichiometric TiB₂ powders with particle sizes < 10 μ m are also acquired from the dynamic air-

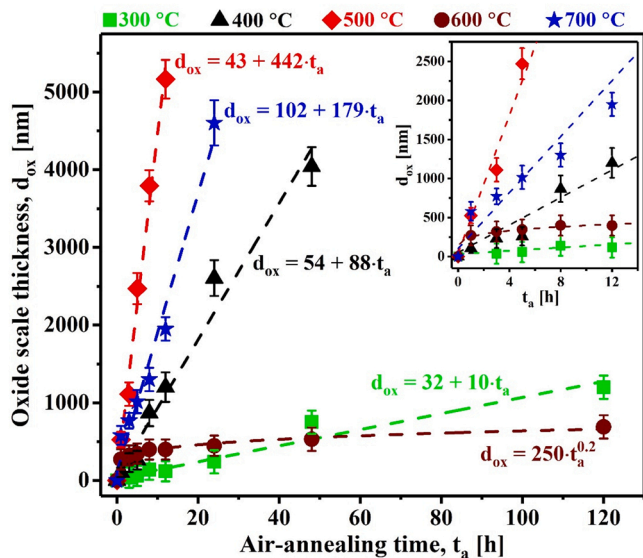


Fig. 12. Thickness of oxide scales d_{ox} formed on the TiB_{2.5} thin films air-annealed at $T_a = 300, 400, 500, 600$, and 700 °C as a function of t_a . No compensation was made for possible B₂O₃ (g) loss or any void fraction in the oxide scale.

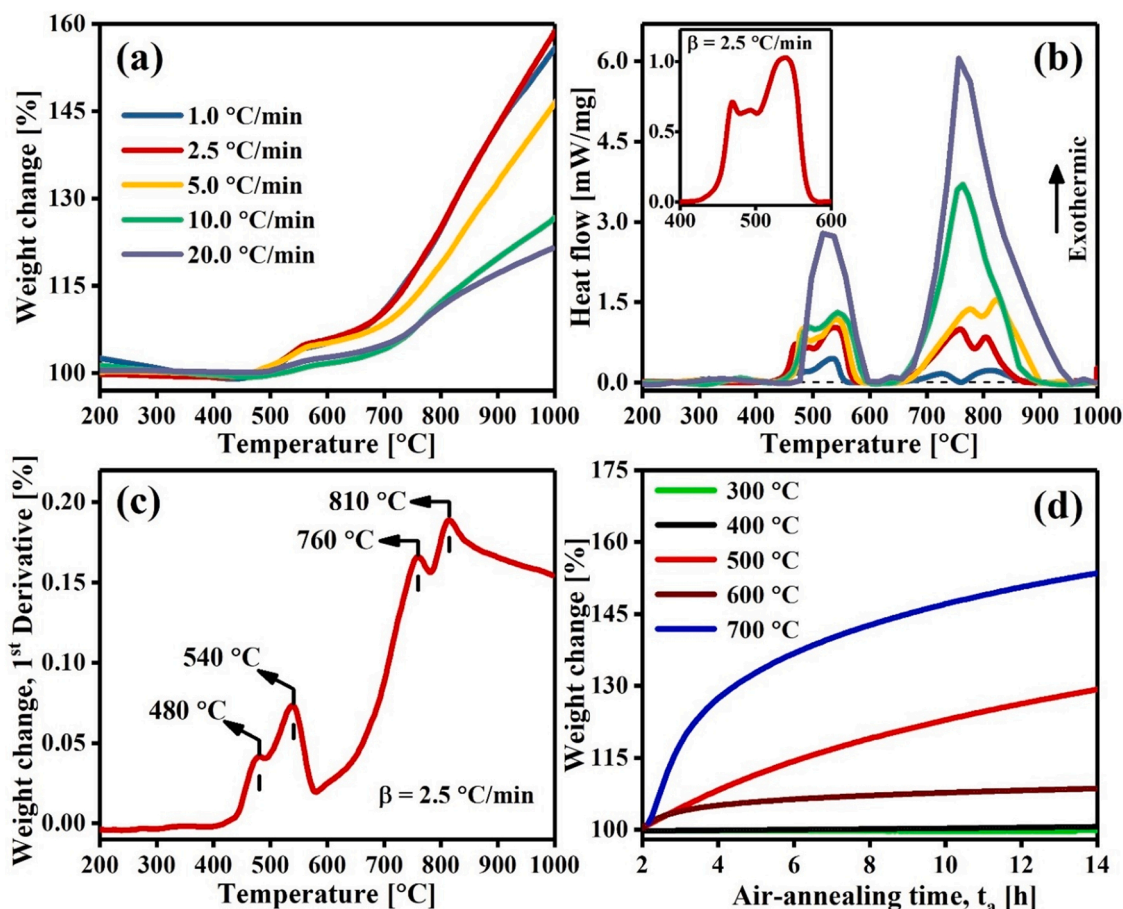


Fig. 13. (a) TG and (b) DSC curves of the $\text{TiB}_{2.5}$ powders acquired from the dynamic air-annealing measurements carried out with heating rates $\beta = 1.0, 2.5, 5.0, 10.0$, and 20.0 $^{\circ}\text{C}/\text{min}$, (c) first derivative of the TG curve for $\beta = 2.5$ $^{\circ}\text{C}/\text{min}$, and (d) TG curves acquired from the isothermal air-annealing measurements with $\beta = 10.0$ $^{\circ}\text{C}/\text{min}$ and $t_a = 12$ h.

Table 1

Oxidation parameters obtained from the TG and DSC curves at different heating rates up to 1000 $^{\circ}\text{C}$.

Reactions set	T_{onset} [$^{\circ}\text{C}$]	T_1 [$^{\circ}\text{C}$]	T_2 [$^{\circ}\text{C}$]	T_3 [$^{\circ}\text{C}$]	T_f [$^{\circ}\text{C}$]	α [%]	ΔH_f [kJ/g]
1	455 ± 19	481 ± 13	500 ± 9	540 ± 4	578 ± 16	5.1 ± 0.5	1.60 ± 0.45
2	662 ± 13	766 ± 10	813 ± 10	–	911 ± 29	44.8 ± 6.2	2.15 ± 0.46

annealing measurements up to 1200 $^{\circ}\text{C}$. Similar to the $\text{TiB}_{2.5}$ powders, the TG curves of the reference TiB_2 powders, shown in [supplementary Fig. S6\(a\)](#), indicate a weight gain trend with $T_{\text{onset}} = 440 \pm 14$ $^{\circ}\text{C}$, which is accompanied by appearing a set of convoluted exothermic signals in their DSC curves, [supplementary Fig. S6\(b\)](#).

The TG results of both reference TiB_2 powders with the particle size < 10 μm and $\text{TiB}_{2.5}$ powders extracted from the thin films do not exhibit any weight loss, which is an indication for the B_2O_3 evaporation [34,77, 78] according to:



This is in contrast to the oxidation behavior of most bulk TMB_2 [34, 37,77,79–81] and coatings [46,78,82] in which the evaporation of B_2O_3 takes place by losing weight. To evaluate the possibility of occurring any change in the weight gain trend at higher temperatures (> 1200 $^{\circ}\text{C}$), the measurements are carried out up to 1500 $^{\circ}\text{C}$ for $\beta = 20.0$ $^{\circ}\text{C}/\text{min}$. However, the result does not show any weight loss at temperatures

> 1200 $^{\circ}\text{C}$. Instead, even a higher weight gain rate is observed at temperatures ≥ 1280 $^{\circ}\text{C}$ that indicates a more rapid oxidation, see [supplementary Fig. S6\(a\)](#). In addition, compared to the DSC data of the $\text{TiB}_{2.5}$ powders in [Fig. 13\(b\)](#) that have two sets of convoluted signals, the DSC curves of the reference TiB_2 powders contain just one set of convoluted signals appearing at temperatures between 440 ± 14 $^{\circ}\text{C}$ and 700 ± 32 $^{\circ}\text{C}$, see [supplementary Fig. S6\(b\)](#).

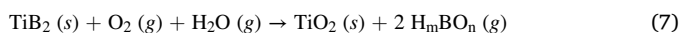
[Fig. 13\(d\)](#) comprises the TG curves of the $\text{TiB}_{2.5}$ powders acquired from the isothermal air-annealing measurements with $\beta = 10.0$ $^{\circ}\text{C}/\text{min}$. The weight change after air-annealing at $T_a = 300$ and 400 $^{\circ}\text{C}$ for $t_a = 12$ h is negligible. However, the powders isothermally air-annealed at $T_a = 500, 600$, and 700 $^{\circ}\text{C}$ gain weight with rates that are higher during the first 3-h air-annealing period than for $t_a > 3$ h. After 12-h isothermal air-annealing, the α values for $T_a = 500, 600$, and 700 $^{\circ}\text{C}$ are 30%, 9%, and 54%, respectively. The apparent difference between the data in [Fig. 12](#) and [Fig. 13\(d\)](#) is due to the fact that the details in [Fig. 12](#) show the oxide-scale thickness changes, while those in [Fig. 13\(d\)](#) exhibit the variations in the oxide-scale weight as a function of t_a . For instance, the oxide scales formed at $T_a = 500$ $^{\circ}\text{C}$ are thicker than those at $T_a = 700$ $^{\circ}\text{C}$, whereas the weight gain at 700 $^{\circ}\text{C}$ is larger than 500 $^{\circ}\text{C}$ that is due to the higher density of rutile phase than anatase phase (rutile- TiO_2 density is 4.24 g/cm^3 , while anatase- TiO_2 density is 3.90 g/cm^3 [60]).

4. Discussion

The employed SEM, XRD, XPS, ToF-ERDA, HAADF-STEM, SAED, EELS, TG, and DSC analyses provide comprehensive data on the chemistry and microstructure of the oxidation products formed on the $\text{TiB}_{2.5}$

thin films after air-annealing at $T_a = 300, 400, 500, 600,$ and 700°C for t_a up to 120 h. Before interpreting the oxidation kinetics of our films, we re-collect what literature stipulates about bulk diboride oxidation. At $T_a \leq 1000^\circ\text{C}$, the oxidation products of bulk TiB_2 consist of porous, crystalline TiO_2 (s) and glassy, amorphous B_2O_3 (l) phases [33,34]. Since the volume of B_2O_3 (l) is greater, the immiscible B_2O_3 (l) phase is typically forced toward the oxide scale's surface, forms a continuous layer, and acts as oxidation barrier [34,36,37]. Thus, at $T_a \leq 1000^\circ\text{C}$, the oxidation rate should be controlled by the oxygen diffusion through this protective B_2O_3 (l) layer [38]. However, our XPS, ToF-ERDA, and EELS results, see Figs. 6, 7, 8, 9, and 11, rather show that the oxide scales forming on the $\text{TiB}_{2.5}$ thin films are highly B-deficient for $T_a \geq 500^\circ\text{C}$, and mainly consist of a TiO_2 skeleton. The average B concentrations in the scales formed after air-annealing at $T_a = 500, 600,$ and 700°C are 1.1 ± 0.2 at%, 0.4 ± 0.1 at%, and 0.2 ± 0.1 at%, respectively. In addition, the TG curves in Fig. 13(a) and 13(c) do not exhibit unbalanced weight loss by the sole evaporation of B_2O_3 (l) [83]. Thus, there is more complexity involved in the oxidation of the $\text{TiB}_{2.5}$ thin films, as from the weight gain during TiO_2 formation.

To understand the underlaying mechanisms for the absence of the B_2O_3 phase in our sputter-deposited thin films, we evaluate the influence of critical parameters such as air-annealing temperature T_a , the presence of water vapor in atmosphere, and the films' chemical composition and nanostructure [16,39–43,84]. At constant oxygen partial pressure, B_2O_3 evaporates as rapidly as it forms at $T_a \geq 1000^\circ\text{C}$ [33,34,40], mostly with a sublimation reaction. However, at low temperatures ($T_a < 1000^\circ\text{C}$), B_2O_3 is highly reactive in atmosphere containing water vapor and rapidly hydrated to H_mBO_n acids (e.g., HBO_2 and H_3BO_3). These two phases can quickly evaporate and/or spall off. Spallation typically takes place due to volume expansion associated with the conversion of the oxide phase to the hydrated form [85–87]. Since the formation of H_mBO_n follows exothermic reactions [83], the additional thermal energy released from these reactions can also to some extent increase temperature and contribute to a higher evaporation rate. The occurrence of such reactions is highly possible for the $\text{TiB}_{2.5}$ thin films as the air-annealing experiments are carried out in a laboratory atmosphere with $\sim 40\%$ humidity. The other factors that can accelerate the evaporation/sublimation of the boron oxide phases in diboride coatings are their chemical composition and nanostructure. As-deposited TiB_x thin films grown by DCMS usually have columnar structure with excess B ($x > 2$) in which the crystalline TiB_2 columns are separated with a thin B-rich tissue phase formed at the column boundaries [25,88]. This phase is amorphous with many more defects than in the crystalline TiB_2 lattice [19]. It was proved that overstoichiometric diborides are more prone to the formation of gaseous boron oxide phases than stoichiometric and understoichiometric ones [16,43] because the vapor pressure of these phases increases as a function of B concentration [42,85]. This implies that the amorphous B-rich column boundaries of sputter-deposited $\text{TiB}_{2.5}$ most likely have higher tendency to form H_mBO_n than the crystalline TiB_2 columns. While the crystalline TiB_2 inside the columns mainly undergoes oxidation according to



reaction, the preferential evaporation of these acids from the column boundaries can follow.



reactions. The formation rate of these gaseous phases at the column boundaries can be more pronounced closer to the surface, where oxygen is supplied, due to a large chemical potential gradient. Therefore, we primarily attribute the absence of the B_2O_3 phase in the air-annealed $\text{TiB}_{2.5}$ thin films to the humid oxidation atmosphere and their special nanostructure.

Fig. 14 compares the schematic cross-sectional illustration of the oxide scales formed on $\text{TiB}_{2.5}$ after air-annealing at $T_a = 300, 400, 500, 600,$ and 700°C . Air-annealing the $\text{TiB}_{2.5}$ thin films up to 400°C results in the formation of amorphous TiO_xB_y oxide scales, see Figs. 3, 5, and 9. Amorphous oxidation products were also observed on bulk TiB_2 air-annealed at $T_a = 400^\circ\text{C}$ [89]. Fig. 8 shows that the B concentration remains almost constant in these oxidation products, while the O and Ti concentrations change with increasing t_a . At $T_a = 300^\circ\text{C}$, $\Psi (\text{B}/(\text{O} + \text{Ti})) = \sim 0.08$ and $\Delta (\text{O}/\text{Ti})$ changes from ~ 2.1 for $t_a = 8$ h to ~ 2.6 for $t_a = 48$ h, while at $T_a = 400^\circ\text{C}$, $\Psi = \sim 0.07$ and Δ increases from ~ 2.4 for $t_a = 8$ h to ~ 2.7 for $t_a = 48$ h. The formation of such amorphous oxide scales can be due to the lack of recrystallization in this temperature range as it is not high enough to crystallize TiO_2 phases [72].

In this regime ($T_a \leq 400^\circ\text{C}$), the oxide-scale growth follows linear oxidation kinetics with an oxidation-rate constant $k = 10$ nm/h for $T_a = 300^\circ\text{C}$ and $k = 88$ nm/h for $T_a = 400^\circ\text{C}$, see Fig. 12. At $T_a = 300^\circ\text{C}$, the XSEM images in Fig. 3(a) to 3(e) and the plan-view EELS elemental maps in Fig. 11(a) and 11(b) show dense scales with an almost uniform distribution of B, O, and Ti. This indicates that such oxidation products could act as oxidation protective barriers, similar to the oxide scales on the bulk diborides [39,40,90]. However, the nanostructural evaluations reveal that the oxide layers formed on the $\text{TiB}_{2.5}$ thin films are porous, and after $d_{\text{ox}} > 750 \pm 70$ nm ($t_a > 48$ h), they also contain some microcracks that form due to residual tensile stresses, which mainly originate from volume expansions accompanied by the formation of boron oxide phases, e.g., the molar volume of B_2O_3 ($27.3 \text{ cm}^3/\text{mol}$ [91]) is approximately twice as high as TiB_2 ($15.4 \text{ cm}^3/\text{mol}$ [91]). When the thickness-stress product of the oxide scale reaches a certain level, the crack formation takes place. Such porous structures also facilitate the inward O_2 (g) and H_2O (g) transfer to unoxidized regions and, hence, the continuous oxidation.

At $T_a = 400^\circ\text{C}$, the plan-view HAADF-STEM micrographs and EELS elemental maps in Fig. 11(c) and 11(d) show open boundaries that form after the formation and evaporation of the boron oxide phases from the B-rich column boundaries of $\text{TiB}_{2.5}$ and act as preferred channels for oxygen transfer. In addition, SEM images in Fig. 3(i), 3(j), 4(i), and 4(j) indicate some deep cracks in the oxide scales with $d_{\text{ox}} > 1200 \pm 90$ nm ($t_a > 12$ h) that can form due to the residual tensile stresses, similar to 300°C . Thus, both open boundaries and deep cracks transfer oxygen to the unoxidized $\text{TiB}_{2.5}$ film and lead to a linear oxide-scale growth at $T_a = 400^\circ\text{C}$. These results, however, are in contrast to the oxidation properties of bulk TiB_2 synthesized by an arc melting process. Cai et al. [89] showed that the oxide scales formed on bulk TiB_2 after air-annealing at 400°C have a protective effect and follow a nonlinear growth ($d_{\text{ox}} = k \cdot t_a^{0.3}$).

Air-annealing the $\text{TiB}_{2.5}$ thin films at $T_a = 500^\circ\text{C}$ leads to the formation of anatase- TiO_2 oxidation products that are highly porous and contain deep, wide cracks. The crack width considerably increases with increasing t_a . Opposite to $T_a = 300$ and 400°C , the average O and Ti concentrations in these oxide layers do not change as a function t_a (O/Ti ratio = ~ 2). The XSEM-obtained thicknesses of the oxide scales d_{ox} , Fig. 12, show that the $\text{TiB}_{2.5}$ thin films follow unprotective linear oxidation kinetics at $T_a = 500^\circ\text{C}$, with an oxidation-rate constant ($k = 442$ nm/h) that is significantly higher than even that at $T_a = 700^\circ\text{C}$ ($k = 179$ nm/h). A similar rapid oxidation behavior was reported for bulk TiB_2 , but with a different oxide-scale structure and chemistry [89]. The scales formed on the sputter-deposited $\text{TiB}_{2.5}$ thin films have two layers; a top porous layer composed of nodular grains, and an inner layer with porosity and large voids that consists of cubic-shape crystallites. Both layers are crystalline and highly B-deficient, see Figs. 8, 9(c), 11(e), and 11(f). However, the top layer in the oxide scales formed on bulk TiB_2 at 500°C comprises crystalline TiO_2 nanograins in an amorphous B_2O_3 matrix, while the inner layer is a fully amorphous TiO_xB_y phase [89]. Both layers in the scales formed on bulk TiB_2 are significantly dense compared to those on sputter-deposited

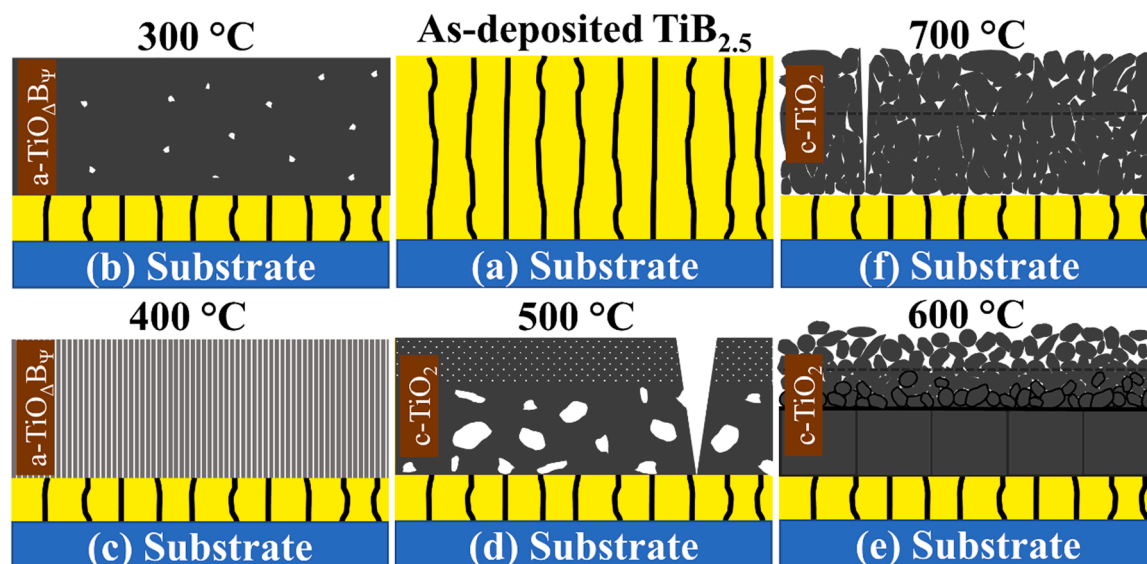


Fig. 14. Cross-sectional illustration of (a) as-deposited $\text{TiB}_{2.5}$ thin film together with oxide scales formed at $T_a =$ (b) 300, (c) 400, (d) 500, (e) 600, and (f) 700 °C. As-deposited $\text{TiB}_{2.5}$ has a columnar nanostructure with B-rich column boundaries, indicated with vertical black lines. The scales formed at 300 and 400 °C have amorphous $\text{a-TiO}_\Delta\text{B}_\psi$ phase, while those formed at 500, 600, and 700 °C have crystalline c-TiO_2 phase. At 600 °C, there is a region between both sublayers that is amorphous, highlighted in black.

$\text{TiB}_{2.5}$

We attribute this extremely rapid oxidation rate to the formation of highly porous oxidation products that contain large voids and deep, wide cracks. These voids and cracks form due mainly to a large volume expansion associated with the anatase transformation (the molar volume of anatase is $20.5 \text{ cm}^3/\text{mol}$ [91]) and the conversion of the oxide phase to H_mBO_n . The formation of such defects is also observed in different bulk Ti-based ceramics oxidized at low temperatures (< 900 °C) [92–96]. It may be interpreted that these cracks form during cooling the samples due to thermal stresses arising from the thermal expansion α mismatch between oxide scales and Si substrate/unoxidized $\text{TiB}_{2.5}$ layers ($\alpha_{\text{anatase-TiO}_2} = 7.8 \times 10^{-6} \text{ K}^{-1}$, $\alpha_{\text{TiB}_2} = 7.0 \times 10^{-6} \text{ K}^{-1}$, and $\alpha_{\text{Si}} = 3.6 \times 10^{-6} \text{ K}^{-1}$ [60]). To examine this possibility, $\text{TiB}_{2.5}$ is grown on a sapphire substrate ($\alpha_{\text{sapphire}} = 7.1\text{--}8.3 \times 10^{-6} \text{ K}^{-1}$ [60]) and air-annealed at $T_a = 500$ °C for 5 h. The plan-view SEM image acquired from this air-annealed sample, shown in [supplementary Fig. S7](#), indicates the presence of similar cracks proving that these cracks, which develop as a function of t_a , primarily form during oxidation process. The oxide-scale growth at $T_a = 500$ °C is likely controlled by the reaction rate at the oxide/film interface, where every oxygen molecule incident on the surface reacts with the diboride [85].

Opposite to our oxidation mechanism, the poor oxidation resistance of bulk TiB_2 at $T_a = 500$ °C was associated to the rapid oxygen diffusion along the interfaces between B_2O_3 and TiO_2 phases in the top layer, rather than inside these phases as they are oxidation resistant at low temperatures, as well as the unprotective effect of the amorphous inner layer at 500 °C [89]. This discrepancy is mainly due to the differences between the structure and chemistry of the oxide scales formed on bulk TiB_2 and sputter-deposited $\text{TiB}_{2.5}$ thin films.

After annealing at $T_a = 600$ °C, the oxide scales, which have a TiO_2 chemistry, contain no crack and are composed of two layers: an outer layer consisting of equiaxed crystallites and a dense inner layer, [Fig. 3\(n\)](#) to [3\(r\)](#). The HAADF-XTEM micrograph and EELS elemental maps in [Fig. 9\(d\)](#) indicate that the outer layer is highly porous and the inner layer consists of two sublayers. The sublayer near the outer layer (equiaxed crystallites) is mostly composed of small round-shape grains, while the one close to the oxide/film interface has columnar grains. Different to the oxide layers formed after air-annealing at $T_a = 300, 400, 500$, and 700 °C that show linear oxidation kinetics, the oxide-scale growth follows $d_{\text{ox}} = 250 \cdot t_a^{0.2}$ relationship at $T_a = 600$ °C. In addition, the TG and

DSC curves in [Fig. 13\(a\)](#) and [13\(b\)](#) exhibit that air-annealing at temperatures between 578 ± 16 °C and 662 ± 13 °C does not lead to a significant weight change and appearing DSC signals. A low oxidation rate was observed in bulk TiB_2 air-annealed at 600 °C with a heating rate β of 10.0 °C/min ($d_{\text{ox}} = k \cdot t_a^{0.3}$), in which the oxide scales consist of a thick amorphous B_2O_3 layer on top of a crystalline TiO_2 inner layer [89].

Next, we suggest a model for the abnormally retarded oxide growth observed at $T_a = 600$ °C. The evolution of the oxide scale on the $\text{TiB}_{2.5}$ thin films during air-annealing at 600 °C is schematically illustrated in [Fig. 15](#). In the beginning of the oxidation process ($t_a < 30$ min), the oxide scale is mainly composed of equiaxed TiO_2 crystallites with large gaps in-between that allow air to readily access the unoxidized regions. At this stage, H_mBO_n easily evaporates, and the oxide growth is limited by the reaction rate at the oxide/film interface. The thickness of this porous layer does not significantly change as a function of t_a (for $t_a \geq 30$ min); however, a new type of layer forms underneath, see [Figs. 3 and 15](#). It consists of small round-shape TiO_2 grains that undergo coarsening during oxidation, resulting in considerably smaller gaps between them. The TiO_2 grains mainly formed at the oxide/film interface are surrounded by amorphous H_mBO_n . The presence of these acids can be primarily attributed to the narrow gaps between the TiO_2 grains that limits the H_mBO_n evaporation as well as a continuous feeding of this region with B from the oxide/film interface (in particular, from the B-rich column boundaries). The latter leads to a continuous H_mBO_n formation at the interface, resulting in a thin amorphous area that can to some extent limit oxygen transfer. The remnants of amorphous H_mBO_n are proved by the HR-XTEM micrographs in [Fig. 10\(b\)](#) and [10\(c\)](#). While we could not access any phase diagram for $\text{TiO}_2\text{--H}_m\text{BO}_n$ and $\text{TiO}_2\text{--B}_2\text{O}_3$, it is now known that the observed amorphous phase is formed in the solid phase at $T_a = 600$ °C or quenched from the liquid state.

By increasing t_a , another new oxide layer forms under the amorphous area that has a completely different structure than the outer oxide layers. This layer consists of TiO_2 grains that preferentially grow toward the film/substrate interface in the [001] direction and form wider columns than as-deposited $\text{TiB}_{2.5}$. The XSEM-obtained thicknesses of the oxide scales d_{ox} shown in [Fig. 12](#) indicate that the oxide scales formed at 600 °C up to $t_a = 1$ h have better oxidation protection than those formed at $T_a = 500$ and 700 °C, while this effect is worse than those formed at $T_a = 300$ and 400 °C. This can be attributed to the porous/open boundaries of the columnar TiO_2 grains, see [Fig. 15](#). However, as schematically

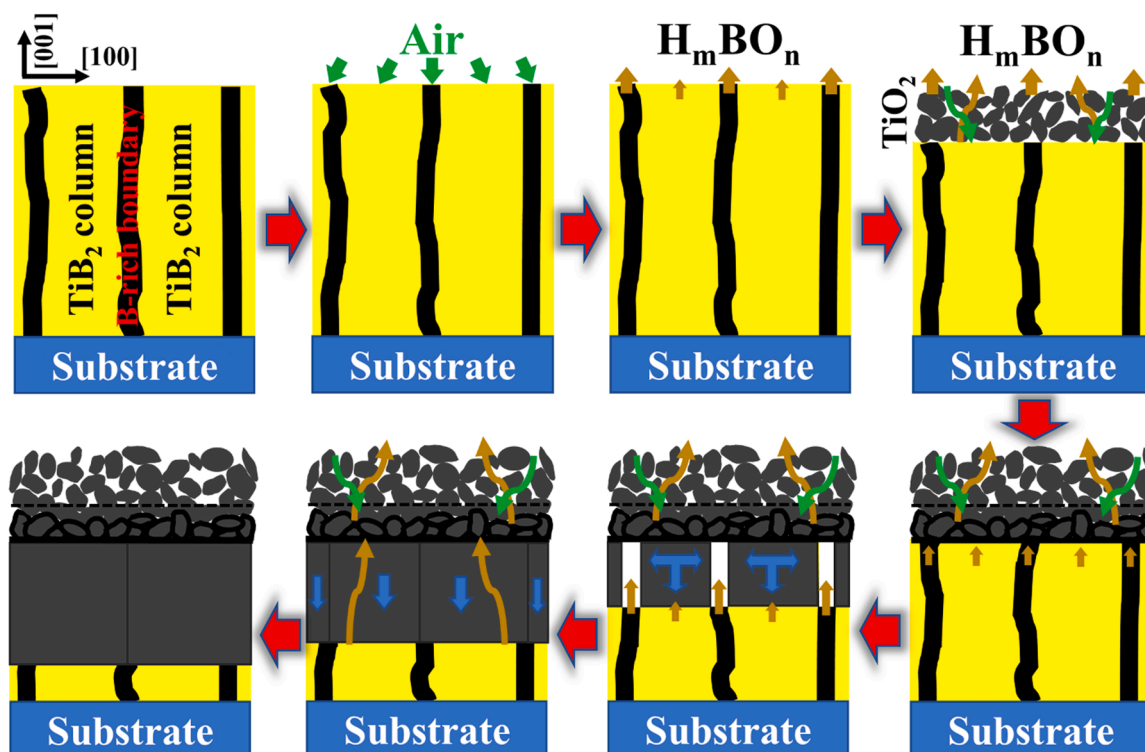


Fig. 15. Schematic cross-sectional illustration of the evolution of the oxide scale formed on $\text{TiB}_{2.5}$ during air-annealing at $T_a = 600^\circ\text{C}$. The TiO_2 grains in the top sublayer are surrounded by an amorphous phase. There is also a thin amorphous layer at the interface between top and bottom sublayers. The amorphous phase is indicated in black.

illustrated in Fig. 15, the TiO_2 columns grow both vertically and laterally for $t_a > 1$ h, resulting in the formation of highly dense column boundaries, see Fig. 10(a). Although the columnar TiO_2 grains are also observed in oxidized bulk diborides [34,97], it is unknown why these grains tend to grow preferentially in one direction. We speculate this columnar growth may be attributed to the restricted TiO_2 grain coarsening in the lateral [100] direction. At this air-annealing regime, the oxidation temperature ($T_a = 600^\circ\text{C}$) is well below the melting-point temperature of TiO_2 (1855°C [60]). Thus, recrystallization effects (here, in particular, grain coarsening in the lateral direction) that typically occur at the homologous temperature $T_h > \sim 0.5$ [64] are highly limited since $T_h = \sim 0.3$ at 600°C . Therefore, when the lateral growth of the TiO_2 grains is completed, the column boundaries are fastened, become highly dense, and do not move further in the [100] direction, while the grain growth continues in the [001] direction toward the unoxidized $\text{TiB}_{2.5}$ film.

In contrast to the outer layer (equiaxed crystallites), the thickness of this oxide layer increases as a function of t_a . Since B has a small atomic size [60], it can easily undergo an outward diffusion (from the columnar oxide layer toward the amorphous interface) mainly through the defects in the TiO_2 lattice, resulting in a B-deficient/free columnar TiO_2 sublayer and continuously feeding the amorphous interface. This dense structure can significantly decrease oxygen transfer toward the unoxidized $\text{TiB}_{2.5}$. Therefore, the oxidation kinetics at $T_a = 600^\circ\text{C}$ are largely limited by the oxygen diffusion through the dense columnar TiO_2 grains and the amorphous thin layer formed between the sublayers.

The effectiveness of this oxidation-barrier sublayer is further examined by conducting two-step air-annealing experiments, schematically illustrated in supplementary Fig. S8. In the first step, $\text{TiB}_{2.5}$ is air-annealed with a heating rate β of $10.0^\circ\text{C}/\text{min}$ and held at $T_a = 600^\circ\text{C}$ for $t_a = 3$ h. Immediately afterward (second step), T_a is decreased to 500°C with $\beta = 10.0^\circ\text{C}/\text{min}$, and the sample is air-annealed at this temperature for $t_a = 3$ h and finally cooled down to room temperature with a rate of $10.0^\circ\text{C}/\text{min}$. In a separate experiment, in the second step,

T_a is increased to 700°C with $\beta = 10.0^\circ\text{C}/\text{min}$, and the sample experiences a 3-h air-annealing at this temperature. Surprisingly, the oxide scale formed at the $[(600^\circ\text{C} - 3\text{ h}) + (500^\circ\text{C} - 3\text{ h})]$ condition has a similar morphology and a comparable average thickness to the scale formed after one-step air-annealing at $T_a = 600^\circ\text{C}$ for $t_a = 3$ h. It has two layers: an outer layer consisting of equiaxed crystallites and a dense inner layer with absolutely no crack, supplementary Fig. S9. Even after 5-h air-annealing at $T_a = 500^\circ\text{C}$, both morphology and thickness of the scale do not significantly change. This two-step air-annealing experiment clearly reveals that the second oxidation step at $T_a = 500^\circ\text{C}$, which is a temperature leading to an extremely fast oxide growth rate in the typical one-step air-annealing, does not result in any further oxidation, proving the oxidation protection effect of the dense columnar TiO_2 sublayer formed at $T_a = 600^\circ\text{C}$.

However, the $[(600^\circ\text{C} - 3\text{ h}) + (700^\circ\text{C} - 3\text{ h})]$ experiment shows that this protection effect depends on T_a in the second oxidation step as it leads to the formation of an oxide scale that has a similar morphology to the scale formed after one-step air-annealing at $T_a = 700^\circ\text{C}$ for $t_a = 3$ h, see Fig. 3(s) and supplementary Fig. S9. This scale also consists of some cracks. Although the oxidation protection effect of the sublayer formed at $T_a = 600^\circ\text{C}$ is not fully preserved during the second oxidation step at $T_a = 700^\circ\text{C}$ due mainly to crystallite coarsening and crack formation (discussed more in the next paragraph), the oxide scale formed in this two-step air-annealing experiment is thinner (670 ± 43 nm) than the scale formed after one-step air-annealing at $T_a = 700^\circ\text{C}$ for $t_a = 3$ h (785 ± 39 nm).

The oxide layers formed on $\text{TiB}_{2.5}$ after air-annealing at $T_a = 700^\circ\text{C}$ have two distinct regions. The top layer consists of loosely-attached sub-micrometer crystallites that are similar to those formed at 600°C , but they undergo significant coarsening, and the highly porous inner layer that has elongated grains with different sizes and shapes. The scales also have deep cracks due to the molar volume expansion (the molar volume of rutile is $18.8\text{ cm}^3/\text{mol}$ [91]), but they are not as wide as those formed at $T_a = 500^\circ\text{C}$. These scales have a randomly-oriented rutile crystal

structure with the TiO_2 chemistry. The crystallites formed at the oxidation front follow Ostwald ripening through the diffusive transfer of material that varies as a function of time [98] and results in the coarsening of the crystallites toward the scale surface. Moreover, the TMO_2 (s) skeletons are typically anion deficient (containing a high concentration of oxygen vacancies) and exhibit a significant oxygen diffusivity tendency [80]. Thus, this coarsening is accompanied by enlarging the porosity between the elongated grains due to a decrease in their surface to volume ratio. Therefore, air-annealing at $T_a = 700^\circ\text{C}$ leads to the formation of oxide scales with a high population of active pathways for the transport of species taking part in the oxidation reaction, causing a linear oxide-scale growth with a high oxidation-rate constant ($k = 179\text{ nm/h}$), Fig. 12.

The effect of thermal history (heating-up duration from room temperature to T_a) on both morphology and thickness of the oxide scales are also evaluated with two different sets of experiments; (i) air-annealing using $\beta = 5.0$ and 1.0°C/min and (ii) direct air-annealing at T_a (the samples do not experience the heating-up duration). Decreasing the heating rate β from 10.0° to 1.0°C/min significantly influence on the oxide scales. For $\beta \geq 5.0^\circ\text{C/min}$, the oxide-scale growth and morphology are not considerably affected by the thermal history before reaching T_a . However, the oxide scales formed at $T_a = 600$ and 700°C with $\beta = 1.0^\circ\text{C/min}$ have outer layers that are similar to the ones formed at $T_a = 500^\circ\text{C}$ (supplementary Fig. S10), while the inner layers appear similar to those formed at $T_a = 600/700^\circ\text{C}$ (depending on oxidizing temperature). In addition, direct air-annealing does not show a noticeable effect on both oxide-scale morphology and thickness. The results convincingly demonstrate that the oxide-scale growth at each T_a is almost independent from the heating-up duration for $\beta \geq 5.0^\circ\text{C/min}$.

5. Conclusion

We study the oxidation properties and kinetics of sputter-deposited $\text{TiB}_{2.5}$ thin films up to 700°C in air for annealing times t_a ranging from 1 to 120 h. The as-deposited film has a hexagonal AlB_2 -crystal structure with a columnar nanostructure in which the column boundaries are B-rich. $\text{TiB}_{2.5}$ shows unprotective linear oxidation kinetics $d_{ox} = a + k \cdot t_a$ at $T_a = 300, 400, 500$, and 700°C with oxidation-rate constant $k = 10, 88, 442$, and 179 nm/h , respectively; however, the oxide layer formed after air-annealing at $T_a = 600^\circ\text{C}$ follows $d_{ox} = 250 \cdot t_a^{0.2}$ growth relationship, which indicates an oxidation protective behavior. The oxide scales formed on $\text{TiB}_{2.5}$ are highly B-deficient for $T_a \geq 500^\circ\text{C}$ and mainly composed of a TiO_2 skeleton. The absence of the B_2O_3 phase is primarily attributed to the humid oxidation atmosphere where B_2O_3 is rapidly hydrated to H_mBO_n acids, which can quickly evaporate and spall off, as well as the special nanostructure of $\text{TiB}_{2.5}$. The structure of oxide scales changes from amorphous to crystalline at temperatures $\geq 500^\circ\text{C}$. TG and DSC analyses reveal a weight-gain trend with two significant parts; one occurs from 455 ± 19 – $578 \pm 16^\circ\text{C}$, and one takes place from 662 ± 13 – $911 \pm 29^\circ\text{C}$. Each event is accompanied by appearing convoluted exothermic signals in the DCS curves, indicating that the $\text{TiB}_{2.5}$ thin films undergo complex oxidation processes. The extremely rapid oxidation rate at $T_a = 500^\circ\text{C}$ is attributed to the formation of large voids and deep, wide cracks in the oxide scales. However, the abnormally low oxidation rate at $T_a = 600^\circ\text{C}$ is due to a highly dense columnar TiO_2 sublayer that forms near the oxide/film interface with a top amorphous thin layer ($< 5\text{ nm}$), which both significantly suppress the oxygen diffusion. We propose a model that explains the abnormally-reduced oxide-scale evolution at 600°C as a function of t_a . The scale formed at 600°C can maintain its oxidation protection at $T_a \leq 500^\circ\text{C}$, but not at $T_a = 700^\circ\text{C}$. Decreasing the heating rate β from 10.0° to 1.0°C/min has a significant influence on the $\text{TiB}_{2.5}$ oxidation. The oxide-scale growth and morphology are not significantly influenced by thermal history (heating-up duration from room temperature to T_a) for $\beta \geq 5.0^\circ\text{C/min}$. We believe the protective oxidation behavior observed at 600°C (with

$\beta \geq 5.0^\circ\text{C/min}$) can offer possibilities for the use of $\text{TiB}_{2.5}$ as protective coatings for applications at this oxidation condition.

CRedit authorship contribution statement

Samira Dorri: Conceptualization, Investigation, Formal analysis, Writing – original draft. **Justinas Palisaitis:** Conceptualization, Investigation, Writing – review & editing. **Grzegorz Greczynski:** Conceptualization, Writing – review & editing. **Ivan Petrov:** Conceptualization, Writing – review & editing. **Jens Birch:** Conceptualization, Supervision, Writing – review & editing. **Lars Hultman:** Conceptualization, Funding acquisition, Writing – review & editing. **Babak Bakht:** Project administration, Supervision, Conceptualization, Investigation, Funding acquisition, Writing – review & editing.

Declaration of Competing Interest

The authors declare that they have no known competing financial interests or personal relationships that could have appeared to influence the work reported in this paper.

Data Availability

Data will be made available on request.

Acknowledgements

The authors gratefully acknowledge William G. Fahrenholtz for useful discussions. Financial support from Swedish Research Council VR Grant numbers 2018-03957, 2019-00191 (for accelerator-based ion-technological center in tandem accelerator laboratory in Uppsala University), and 2021-00357, Swedish Foundation for Strategic Research (SSF), Swedish Government Strategic Research Area in Materials Science on Advanced Functional Materials (AFM) at Linköping University (Faculty Grant SFO Mat LiU No. 2009 00971), Swedish National Graduate School in Neutron Scattering (SwedNess), and Knut and Alice Wallenberg Foundation for the support of electron microscopy laboratory in Linköping University (KAW 2015.0043) are acknowledged.

Appendix A. Supporting information

Supplementary data associated with this article can be found in the online version at doi:10.1016/j.corsci.2022.110493.

References

- [1] N.N. Greenwood, A. Earnshaw, in: N.N. Greenwood, A. Earnshaw (Eds.), *Chemistry of the Elements*, second ed., Butterworth-Heinemann, Oxford, 1997.
- [2] M. Magnuson, L. Hultman, H. Höglberg, Review of transition-metal diboride thin films, *Vacuum* (2021), 110567.
- [3] N.P. Bansal, *Handbook of Ceramic Composites*, Kluwer Academic Publishers, Boston MA, 2005.
- [4] N.L. Okamoto, M. Kusakari, K. Tanaka, H. Inui, S. Otani, Anisotropic elastic constants and thermal expansivities in monocrystal CrB_2 , TiB_2 , and ZrB_2 , *Acta Mater.* 58 (1) (2010) 76–84.
- [5] V.I. Matkovich, G.V. Samsonov, P. Hagenmuller, T. Lundström, Boron and Refractory Borides, Springer-Verlag, Berlin, 1977.
- [6] L. Benko, T. Lundström, The high-temperature hardness of ZrB_2 and HfB_2 , *J. Less Common Met* 34 (2) (1974) 273–278.
- [7] V. Moraes, C. Fuger, V. Paneta, D. Primetzhöfer, P. Polcik, H. Bolvardi, M. Arndt, H. Riedl, P.H. Mayrhofer, Substoichiometry and tantalum dependent thermal stability of α -structured W-Ta-B thin films, *Scr. Mater.* 155 (2018) 5–10.
- [8] J.C. Zhao, J.H. Westbrook, Ultrahigh-temperature materials for jet engines, *MRS Bull.* 28 (9) (2003) 622–630.
- [9] F. Monteverde, L. Scatteia, Resistance to thermal shock and to oxidation of metal diborides-SiC, *Ceram. Aerosp. Appl. J. Am. Ceram. Soc.* 90 (4) (2007) 1130–1138.
- [10] T. Shikama, T. Noda, M. Fukutomi, M. Okada, Deuterium retention in $\text{Ti}_{1-x}\text{B}_x$ films deposited onto molybdenum by co-sputtering method, *J. Nucl. Mater.* 141–143 (1986) 156–159.
- [11] W.G. Fahrenholtz, G.E. Hilmas, Ultra-high temperature ceramics: Materials for extreme environments, *Scr. Mater.* 129 (2017) 94–99.

- [12] M.A. Nicolet, Diffusion barriers in thin films, *Thin Solid Films* 52 (3) (1978) 415–443.
- [13] G. Sade, J. Pelleg, Co-sputtered TiB₂ as a diffusion barrier for advanced microelectronics with Cu metallization, *Appl. Surf. Sci.* 91 (1) (1995) 263–268.
- [14] J. Sung, D.M. Goedde, G.S. Girolami, J.R. Abelson, Remote-plasma chemical vapor deposition of conformal ZrB₂ films at low temperature: A promising diffusion barrier for ultralarge scale integrated electronics, *J. Appl. Phys.* 91 (6) (2002) 3904–3911.
- [15] M. Audronis, A. Leyland, A. Matthews, J.G. Wen, I. Petrov, Characterization studies of pulse magnetron sputtered hard ceramic titanium diboride coatings alloyed with silicon, *Acta Mater.* 56 (16) (2008) 4172–4182.
- [16] B. Bakht, J. Palisaitis, J. Thörnberg, J. Rosen, P.O.Å. Persson, L. Hultman, I. Petrov, J.E. Greene, G. Greczynski, Improving the high-temperature oxidation resistance of TiB₂ thin films by alloying with Al, *Acta Mater.* 196 (2020) 677–689.
- [17] B. Bakht, D.L.J. Engberg, J. Lu, J. Rosen, H. Högborg, L. Hultman, I. Petrov, J. E. Greene, G. Greczynski, Strategy for simultaneously increasing both hardness and toughness in ZrB₂-rich Zr_{1-x}Ta_xBy thin films, *J. Vac. Sci. Technol. A* 37 (3) (2019), 031506.
- [18] B. Bakht, I. Petrov, J.E. Greene, L. Hultman, J. Rosén, G. Greczynski, Controlling the B/Ti ratio of TiB_x thin films grown by high-power impulse magnetron sputtering, *J. Vac. Sci. Technol.* 36 (3) (2018), 030604.
- [19] B. Bakht, J. Palisaitis, Z. Wu, M.A. Sortica, D. Primetzhof, P.O.Å. Persson, J. Rosen, L. Hultman, I. Petrov, J.E. Greene, G. Greczynski, Age hardening in superhard ZrB₂-rich Zr_{1-x}Ta_xBy thin films, *Scr. Mater.* 191 (2021) 120–125.
- [20] T. Leyendecker, O. Lemmer, S. Esser, J. Ebberink, The development of the PVD coating TiAlN as a commercial coating for cutting tools, *Surf. Coat. Technol.* 48 (2) (1991) 175–178.
- [21] B. Subramanian, C.V. Muraleedharan, R. Ananthakumar, M. Jayachandran, A comparative study of titanium nitride (TiN), titanium oxy nitride (TiON) and titanium aluminum nitride (TiAlN), as surface coatings for bio implants, *Surf. Coat. Technol.* 205 (21) (2011) 5014–5020.
- [22] L.E. Toth, *Transition Metal Carbides and Nitrides*, Academic Press, NY, 1971.
- [23] O. Knotek, M. Böhmer, T. Leyendecker, On structure and properties of sputtered Ti and Al based hard compound films, *J. Vac. Sci. Technol.* 4 (6) (1986) 2695–2700.
- [24] A. Kirnbauer, A. Wagner, V. Moraes, D. Primetzhof, M. Hans, J.M. Schneider, P. Polcik, P.H. Mayrhofer, Thermal stability and mechanical properties of sputtered (Hf,Ta,V,W,Zr)-diborides, *Acta Mater.* 200 (2020) 559–569.
- [25] P.H. Mayrhofer, C. Mitterer, J.G. Wen, J.E. Greene, I. Petrov, Self-organized nanocolumnar structure in superhard TiB₂ thin films, *Appl. Phys. Lett.* 86 (13) (2005), 131909.
- [26] S. Guo, H. Sun, Superhardness induced by grain boundary vertical sliding in (001)-textured ZrB₂ and TiB₂ nano films, *Acta Mater.* 218 (2021), 117212.
- [27] W.J. Clegg, Controlling cracks in ceramics, *Science* 286 (5442) (1999) 1097.
- [28] R.O. Ritchie, The conflicts between strength and toughness, *Nat. Mater.* 10 (11) (2011) 817–822.
- [29] B. Bakht, S. Dorri, A. Kooijman, Z. Wu, J. Lu, J. Rosen, J.M.C. Mol, L. Hultman, I. Petrov, J.E. Greene, G. Greczynski, Multifunctional ZrB₂-rich Zr_{1-x}Cr_xBy thin films with enhanced mechanical, oxidation, and corrosion properties, *Vacuum* (2020), 109990.
- [30] B. Bakht, S. Dorri, A. Kosari, A. Mol, L. Hultman, I. Petrov, G. Greczynski, Microstructure, mechanical, and corrosion properties of Zr_{1-x}Cr_xBy diboride alloy thin films grown by hybrid high power impulse/DC magnetron co-sputtering, *Appl. Surf. Sci.* 591 (2022), 153164.
- [31] B. Bakht, J. Palisaitis, P.O.Å. Persson, B. Alling, J. Rosen, L. Hultman, I. Petrov, J. E. Greene, G. Greczynski, Self-organized columnar Zr_{0.7}Ta_{0.3}B_{1.5} core/shell-nanostructure thin films, *Surf. Coat. Technol.* 401 (2020), 126237.
- [32] W.G. Fahrenholtz, G.E. Hilmas, I.G. Talmy, J.A. Zaykoski, Refractory diborides of zirconium and hafnium, *J. Am. Ceram. Soc.* 90 (5) (2007) 1347–1364.
- [33] T.A. Parthasarathy, R.A. Rapp, M. Opeka, R.J. Kerans, A model for the oxidation of ZrB₂, HfB₂ and TiB₂, *Acta Mater.* 55 (17) (2007) 5999–6010.
- [34] Y.H. Koh, S.Y. Lee, H.E. Kim, Oxidation behavior of titanium boride at elevated temperatures, *J. Am. Ceram. Soc.* 84 (1) (2001) 239–241.
- [35] M.M. Opeka, I.G. Talmy, E.J. Wuchina, J.A. Zaykoski, S.J. Causey, Mechanical, thermal, and oxidation properties of refractory hafnium and zirconium compounds, *J. Eur. Ceram. Soc.* 19 (13) (1999) 2405–2414.
- [36] V.A. Lavrenko, S.S. Chuprov, A.P. Umanskii, T.G. Protchenko, E.S. Lugovskaya, High-temperature oxidation of composite materials based on titanium diboride, *Powder Metall. Met. Ceram.* 26 (9) (1987) 761–762.
- [37] H.C. Graham, H.H. Davis, I.A. Kvernes, W.C. Tripp, Microstructural features of oxide scales formed on zirconium diboride materials, in: W.W. Krieger, H. Palmour (Eds.), *Ceramics in Severe Environments*, Springer, US, Boston, MA, 1971.
- [38] B. Basu, G.B. Raju, A.K. Suri, Processing and properties of monolithic TiB₂ based materials, *Int. Mater. Rev.* 51 (6) (2006) 352–374.
- [39] A.K. Kuriakose, J. Margrave, The oxidation kinetics of zirconium diboride and zirconium carbide at high temperatures, *J. Electrochem. Soc.* 111 (7) (1964) 827–831.
- [40] M.M. Opeka, I.G. Talmy, J.A. Zaykoski, Oxidation-based materials selection for 2000 °C + hypersonic aerosurfaces: theoretical considerations and historical experience, *J. Mater. Sci.* 39 (19) (2004) 5887–5904.
- [41] W.G. Fahrenholtz, E.J. Wuchina, W.E. Lee, Y. Zhou, Ultra-high temperature ceramics: materials for extreme environment applications, Wiley, Hoboken, NJ, 2014.
- [42] L. Kaufman, E.V. Clougherty, Investigation of boride compounds for very high temperature applications, RTD-TRD-N63-4096, Part II, ManLabs Inc., Cambridge, MA, 1965.
- [43] J. Thörnberg, B. Bakht, J. Palisaitis, N. Hellgren, L. Hultman, G. Greczynski, P.O.Å. Persson, I. Petrov, J. Rosen, Improved oxidation properties from a reduced B content in sputter-deposited TiB_x thin films, *Surf. Coat. Technol.* 420 (2021), 127353.
- [44] J. Thörnberg, S. Mráz, J. Palisaitis, F.F. Klimashin, P. Ondracka, B. Bakht, P. Polcik, S. Kolozsvári, L. Hultman, I. Petrov, P.O.Å. Persson, J.M. Schneider, J. Rosen, Oxidation resistance and mechanical properties of sputter-deposited Ti_{0.9}Al_{0.1}B_{2-y} thin films, *Surf. Coat. Technol.* 128187 (2022).
- [45] A.H.N. Kashani, S. Mráz, D.M. Holzapfel, M. Hans, L. Löfler, P. Ondracka, D. Primetzhof, J.M. Schneider, Synthesis and oxidation behavior of Ti_{0.35}Al_{0.65}By (y = 1.7–2.4) coatings, *Surf. Coat. Technol.* 128190 (2022).
- [46] T. Glechner, H.G. Oemer, T. Wojcik, M. Weiss, A. Limbeck, J. Ramm, P. Polcik, H. Riedl, Influence of Si on the oxidation behavior of TM-Si-B_{2+z} coatings (TM = Ti, Cr, Hf, Ta, W), *Surf. Coat. Technol.* (2022), 128178.
- [47] C. Rebholz, A. Leyland, J.M. Schneider, A.A. Voevodin, A. Matthews, Structure, hardness and mechanical properties of magnetron-sputtered titanium-aluminum boride films, *Surf. Coat. Technol.* 120–121 (1999) 412–417.
- [48] A. Mockute, J. Palisaitis, B. Alling, P. Berastegui, E. Broitman, L.Å. Näslund, N. Nedfors, J. Lu, J. Jensen, L. Hultman, J. Patscheider, U. Jansson, P.O.Å. Persson, J. Rosen, Age hardening in (Ti_{1-x}Al_x)B_{2+Δ} thin films, *Scr. Mater.* 127 (2017) 122–126.
- [49] A. Mockute, J. Palisaitis, N. Nedfors, P. Berastegui, E. Broitman, B. Alling, L. Å. Näslund, L. Hultman, J. Patscheider, U. Jansson, P.O.Å. Persson, J. Rosen, Synthesis and characterization of (Ti_{1-x}Al_x)B_{2+Δ} thin films from combinatorial magnetron sputtering, *Thin Solid Films* 669 (2019) 181–187.
- [50] M. Stüber, H. Riedl, T. Wojcik, S. Ulrich, H. Leiste, P.H. Mayrhofer, Microstructure of Al-containing magnetron sputtered TiB₂ thin films, *Thin Solid Films* 688 (2019), 137361.
- [51] J. Palisaitis, Use of cleaved wedge geometry for plan-view transmission electron microscopy sample preparation, *Microsc. Res. Tech.* 84 (2021) 3182–3190.
- [52] G.C.A.M. Janssen, M.M. Abdalla, F. van Keulen, B.R. Pujada, B. van Venrooy, Celebrating the 100th anniversary of the Stoney equation for film stress: Developments from polycrystalline steel strips to single crystal silicon wafers, *Thin Solid Films* 517 (6) (2009) 1858–1867.
- [53] G.G. Stoney, C.A. Parsons, The tension of metallic films deposited by electrolysis, *Proceedings of the Royal Society of London. Series A, Containing Papers of a Mathematical and Physical Character* 82(553) (1909) 172–175.
- [54] B. Bakht, D. Primetzhof, E. Pitthan, M.A. Sortica, E. Ntemou, J. Rosen, L. Hultman, I. Petrov, G. Greczynski, Systematic compositional analysis of sputter-deposited boron-containing thin films, *J. Vac. Sci. Technol.* 39 (6) (2021), 063408.
- [55] ISO 15472:2010, “Surface chemical analysis - X-ray photoelectron spectrometers - Calibration of energy scales” (ISO, Geneva, 2010).
- [56] G. Greczynski, L. Hultman, X-ray photoelectron spectroscopy: Towards reliable binding energy referencing, *Prog. Mater. Sci.* 107 (2020), 100591.
- [57] W.C. Oliver, G.M. Pharr, An improved technique for determining hardness and elastic modulus using load and displacement sensing indentation experiments, *J. Mater. Res.* 7 (6) (1992) 1564–1583.
- [58] D.B. Williams, C.B. Carter, *Transmission Electron Microscopy: A Textbook for Materials Science. Diffraction. II*, Springer 1996.
- [59] M. Ohring, *Materials science of thin films*, Academic Press, San Diego, California, 2001.
- [60] W. Martienssen, H. Warlimont, *Springer Handbook of Condensed Matter and Materials Data*, Springer, Heidelberg, Berlin, 2006.
- [61] R.G. Munro, Material properties of titanium diboride, *J. Res. Natl. Inst. Stand. Technol.* 105 (5) (2000) 709–720.
- [62] P. Zaumseil, High-resolution characterization of the forbidden Si 200 and Si₂ 222 Reflect., *J. Appl. Cryst.* 48 (2) (2015) 528–532.
- [63] M. Birkholz, *Thin Film, Analysis by X-Ray Scattering*, Wiley, 2006.
- [64] J.A. Thornton, High rate thick film growth, *Annu. Rev. Mater. Sci.* 7 (1) (1977) 239–260.
- [65] L. Hultman, G. Håkansson, U. Wahlström, J.E. Sundgren, I. Petrov, F. Adibi, J. E. Greene, Transmission electron microscopy studies of microstructural evolution, defect structure, and phase transitions in polycrystalline and epitaxial Ti_{1-x}Al_xN and TiN films grown by reactive magnetron sputter deposition, *Thin Solid Films* 205 (2) (1991) 153–164.
- [66] R.E. Smallman, R.J. Bishop, *Modern Physical Metallurgy and Materials Engineering-Science, process, applications*, Chapter 7, Butterworth-Heinemann Linacre House, Jordan Hill, Oxford, 1999.
- [67] JCPDS International Centre for Diffraction Data, Titanium oxide (TiO₂) card 01-071-1166.
- [68] JCPDS International Centre for Diffraction Data, Titanium Oxide (TiO₂) card 00-004-0551.
- [69] T.B. Ghosh, S. Dhabal, A.K. Datta, On crystallite size dependence of phase stability of nanocrystalline TiO₂, *J. Appl. Phys.* 94 (7) (2003) 4577–4582.
- [70] A. Czanderna, C.R. Rao, J. Honig, The anatase-rutile transition Part I. Kinetics of the transformation of pure anatase, *J. Chem. Soc. Faraday Trans.* 54 (1958) 1069–1073.
- [71] G. Li, L. Li, J. Boerio-Goates, B.F. Woodfield, High purity anatase TiO₂ nanocrystals: near room-temperature synthesis, grain growth kinetics, and surface hydration chemistry, *J. Am. Chem. Soc.* 127 (24) (2005) 8659–8666.
- [72] D.A.H. Hanaor, C.C. Sorrell, Review of the anatase to rutile phase transformation, *J. Mater. Sci.* 46 (4) (2011) 855–874.
- [73] JCPDS International Centre for Diffraction Data, Titanium Diboride (TiB₂) card 00-035-0741.

- [74] G. Greczynski, L. Hultman, M. Odén, X-ray photoelectron spectroscopy studies of $Ti_{1-x}Al_xN$ ($0 \leq x \leq 0.83$) high-temperature oxidation: the crucial role of Al concentration, *Surf. Coat. Technol.* 374 (2019) 923–934.
- [75] G. Greczynski, L. Hultman, Towards reliable X-ray photoelectron spectroscopy: Sputter-damage effects in transition metal borides, carbides, nitrides, and oxides, *Appl. Surf. Sci.* 542 (2021), 148599.
- [76] S. Sarkar, P.K. Das, S. Bysakh, Effect of heat treatment on morphology and thermal decomposition kinetics of multiwalled carbon nanotubes, *Mater. Chem. Phys.* 125 (1) (2011) 161–167.
- [77] J.B. Berkowitz-Mattuck, High-temperature oxidation. III. zirconium and hafnium diborides, *J. Electrochem. Soc.* 113 (9) (1966) 908.
- [78] X. Huang, S. Sun, G. Tu, Investigation of mechanical properties and oxidation resistance of CVD TiB_2 ceramic coating on molybdenum, *J. Mater. Res. Technol.* 9 (1) (2020) 282–290.
- [79] F. Li, Y. Cao, J. Liu, H. Zhang, S. Zhang, Oxidation resistance of ZrB_2 and ZrB_2 -SiC ultrafine powders synthesized by a combined sol-gel and boro/carbothermal reduction method, *Ceram. Inter.* 43 (10) (2017) 7743–7750.
- [80] R. Hassan, K. Balani, Oxidation kinetics of ZrB_2 - and HfB_2 -powders and their SiC reinforced composites, *Corr. Sci.* 177 (2020), 109024.
- [81] B. Shahbahrami, H. Bastami, N. Shahbahrami, Studies on oxidation behaviour of TiB_2 powder, *Mater. Res. Innov.* 14 (1) (2010) 107–109.
- [82] T. Glechner, O.E. Hudak, T. Wojcik, L. Haager, F. Bohrn, H. Hutter, O. Hunold, J. Ramm, S. Kolozsvári, E. Pitthan, D. Primetzhofner, H. Riedl, Influence of the non-metal species on the oxidation kinetics of Hf, HfN, HfC, and HfB_2 coatings, *Mater. Des.* 211 (2021), 110136.
- [83] C. Huber, S. Setoodeh Jahromy, C. Jordan, M. Schreiner, M. Harasek, A. Werner, F. Winter, Boric acid: a high potential candidate for thermochemical energy storage, *Energies* 12 (6) (2019) 1086.
- [84] A. Kulpa, T. Troczynski, Oxidation of TiB_2 powders below $900^\circ C$, *J. Am. Ceram. Soc.* 79 (2) (1996) 518–520.
- [85] L. Kaufman, E.V. Clougherty, Investigation of boride compounds for very high-temperature applications, ManLabs. Inc., Cambridge, Mass., 1963.
- [86] R. Balasubramanian, T.S. Lakshmi Narasimhan, R. Viswanathan, S. Nalini, Investigation of the vaporization of boric acid by transpiration thermogravimetry and knudsen effusion mass spectrometry, *J. Phys. Chem. B* 112 (44) (2008) 13873–13884.
- [87] R. Naraparaju, K. Maniya, A. Murchie, W.G. Fahrenholtz, G.E. Hilmas, Effect of moisture on the oxidation behavior of ZrB_2 , *J. Am. Ceram. Soc.* 104 (2) (2021) 1058–1066.
- [88] J. Neidhardt, S. Mráz, J.M. Schneider, E. Strub, W. Böhne, B. Liedke, W. Möller, C. Mitterer, Experiment and simulation of the compositional evolution of Ti-B thin films deposited by sputtering of a compound target, *J. Appl. Phys.* 104 (6) (2008), 063304.
- [89] X. Cai, S. Ding, K. Wen, L. Xu, H. Xue, S. Xin, T. Shen, Unmasking the anomalous rapid oxidation of refractory TiB_2 , *Low. Temp., J. Eur. Ceram. Soc.* 41 (10) (2021) 5100–5108.
- [90] W.C. Tripp, H.H. Davis, H.C. Graham, Effect of an SiC addition on the oxidation of ZrB_2 , *Am. Ceram. Soc. Bull.* 52 (8) (1973) 612–616.
- [91] H. Goldschmidt, Metal physics of interstitial alloys. Interstitial Alloys, Springer, 1967.
- [92] T.S.R.C. Murthy, R. Balasubramanian, B. Basu, A.K. Suri, M.N. Mungole, Oxidation of monolithic TiB_2 and TiB_2 -20wt% $MoSi_2$ composite at $850^\circ C$, *J. Europ. Ceram. Soc.* 26 (1) (2006) 187–192.
- [93] A. Tampieri, E. Landi, A. Bellosi, On the oxidation behaviour of monolithic TiB_2 and Al_2O_3 - TiB_2 and Si_3N_4 - TiB_2 Compos., *J. Therm. Anal.* 38 (12) (1992) 2657–2668.
- [94] T.S.R.C. Murthy, J.K. Sonber, C. Subramanian, R.K. Fotedar, M.R. Gonal, A.K. Suri, Effect of CrB_2 addition on densification, properties and oxidation resistance of TiB_2 , *Int. J. Refract. Hard. Met* 27 (6) (2009) 976–984.
- [95] S. Shimada, M. Kozeki, Oxidation of TiC at low temperatures, *J. Mater. Sci.* 27 (7) (1992) 1869–1875.
- [96] C. Li, Y. Qian, C. Ma, S. Wang, M. Li, Suppressing the anomalous rapid oxidation of Ti_3AlC_2 by incorporating TiB_2 , *J. Mater. Sci. Technol.* 35 (3) (2019) 432–439.
- [97] G.B. Raju, B. Basu, A.K. Suri, Oxidation kinetics and mechanisms of hot-pressed TiB_2 - $MoSi_2$, *Compos. J. Am. Ceram. Soc.* 91 (10) (2008) 3320–3327.
- [98] C. Herring, W. Kingston, The physics of powder metallurgy, WE Kingston, Edition: McGraw Hill, New York, 1951.